

## Adsorption and photocatalysis compiled toxic dyes mineralization using graphitic carbon nitride modified $\text{ZnFe}_2\text{O}_4$ and $\text{CoFe}_2\text{O}_4$ photocatalysts supported onto N-doped graphene

Naresh Chandel<sup>a</sup>, Sheetal Sharma<sup>a</sup>, Vishal Dutta<sup>a</sup>, Pankaj Raizada<sup>a,b</sup>, Ahmad Hosseini-Bandegharai<sup>c,d</sup>, Rajesh Kumar<sup>e</sup>, Vinod Kumar Gupta<sup>f</sup>, Shilpi Agarwal<sup>f</sup>, Pardeep Singh<sup>a,b,\*</sup>

<sup>a</sup>Faculty of Basic Sciences, School of Chemistry, Shoolini University, Solan (Himachal Pradesh) – 173212, India, emails: pardeepchem@gmail.com (P. Singh), nareshsktchemistry@gmail.com (N. Chandel), sheetalkamalsharma@gmail.com (S. Sharma), vishaldutta60@gmail.com (V. Dutta), pankajchem1@gmail.com (P. Raizada)

<sup>b</sup>Himalayan Centre for Excellence in Nanotechnology, Shoolini University, Solan (HP) India – 173229

<sup>c</sup>Department of Environmental Health Engineering, Faculty of Health, Sabzevar University of Medical Sciences, Sabzevar, Iran, email: ahoseinib@yahoo.com (A. Hosseini-Bandegharai)

<sup>d</sup>Department of Engineering, Kashmar Branch, Islamic Azad University, P.O. Box: 161, Kashmar, Iran

<sup>e</sup>Faculty of Basic Sciences, School of Physics and Material Sciences, Shoolini University, Solan (Himachal Pradesh) – 173212, India, email: rajeshsharma@shooliniuniversity.com (R. Kumar)

<sup>f</sup>Faculty of Science, Center of Excellence for Advanced Materials Research, King Abdulaziz University, Jeddah – 21589, Saudi Arabia, emails: vinodfcy@gmail.com (V.K. Gupta), shilpi.agarwal2307@gmail.com (S. Agarwal)

Received 10 September 2019; Accepted 10 February 2020

### ABSTRACT

The novel attributes of graphitic carbon nitride (GCN), such as non-toxic nature, less cost, simple fabrication, earth abundance, and great chemical resistance have popularized them as multifaceted nanomaterials, as compared to the traditional semiconductors. In present work, GCN modified  $\text{ZnFe}_2\text{O}_4$  (ZF) and  $\text{CoFe}_2\text{O}_4$  (CF) were immobilized onto N-doped graphene (NG) via modified hydrothermal method. GCN/ $\text{ZnFe}_2\text{O}_4$ /NG and GCN/ $\text{CoFe}_2\text{O}_4$ /NG photocatalysts were characterized using advanced spectral techniques viz. High-resolution transmission electron microscopy, scanning electron microscopy, X-ray diffraction, Fourier transform infrared, UV, and X-ray photoelectron spectroscopy. The photocatalytic performance of the fabricated photocatalysts was examined for effective photodegradation of malachite green (MG) and methyl orange (MO) under visible light radiation. The photodegradation of MG within 70 min followed the trend: GCN/ $\text{CoFe}_2\text{O}_4$ /NG (98%) > GCN/ $\text{ZnFe}_2\text{O}_4$ /NG (93%) >  $\text{CoFe}_2\text{O}_4$  (50%) >  $\text{ZnFe}_2\text{O}_4$  (48%) > GCN (46%) > NG (28%). For MO, removal efficiency followed the order after 140 min: GCN/ $\text{CoFe}_2\text{O}_4$ /NG (99%) > GCN/ $\text{ZnFe}_2\text{O}_4$ /NG (96%) >  $\text{CoFe}_2\text{O}_4$  (51%) >  $\text{ZnFe}_2\text{O}_4$  (49%) > GCN (48%) > NG (28%). The degradation rate constants ( $k$ ) for MG degradation using GCN/ $\text{ZnFe}_2\text{O}_4$ /NG and GCN/ $\text{CoFe}_2\text{O}_4$ /NG were 0.032 and 0.034  $\text{min}^{-1}$ , respectively, meanwhile, for MO elimination the obtained rate constants were respectively 0.029 and 0.026  $\text{min}^{-1}$ . The adsorption experiments revealed that the MG maximum adsorption happened at pH 8–9, whereas MO maximum adsorption occurred at pH 4. The formation of intermediates during the photodegradation method was demonstrated by high-performance liquid chromatography and gas chromatography–mass spectrometry analysis. During the recycle experiments, GCN/ $\text{ZnFe}_2\text{O}_4$ /NG and GCN/ $\text{CoFe}_2\text{O}_4$ /NG displayed effectual photodegradation activity, respectively after 10 successive cycles. Due to significant recyclability, GCN/ $\text{ZnFe}_2\text{O}_4$ /NG and GCN/ $\text{CoFe}_2\text{O}_4$ /NG could be used as economical photocatalysts for the wastewater remediation.

**Keywords:**  $\text{ZnFe}_2\text{O}_4$  and  $\text{CoFe}_2\text{O}_4$ ; Graphitic carbon nitride; Supported photocatalysis; Enhanced dye degradation; Quick magnetic recovery; Recyclability

\* Corresponding author.

## 1. Introduction

The ever-growing demand to improve the quality of human lifestyle drastically encourages rapid urbanization and industrialization [1,2]. Mainly, associated with accelerating progress of industrialization, the release of carcinogenic, hazardous, and non-biodegradable dyes in water bodies are constantly deteriorating ecological equilibrium and causes many serious diseases [3–5]. Advanced oxidation processes (AOPs) are attractive wastewater treatment options, originally described as homogeneous methods that produce highly reactive  $\text{OH}^\bullet$ , which has a stronger oxidation potential ( $\approx 2.8$  eV) in water and oxidize noxious organic contaminants under climatic conditions [6–9]. However, AOPs suffer several roadblocks such as high cost, comparatively complicated operations, and harsh reactive conditions. AOPs relying on heterogeneous photocatalysis to accelerate pollutant degradation through the utilization of renewable solar energy with precise focus on current limitations has been considered as one of the paramount advantageous strategies [10–12]. Heterogeneous photocatalysis is considered as a green strategy for remediation of wastewater due to several advantages and leads to formation of innocuous products, in which reaction conditions are mild and less chemical input is needed [13–16]. The mechanism of photocatalysis implicate two events where the first event comprises oxidation of absorbed  $\text{H}_2\text{O}$  by photogenerated holes and second includes reduction of dissolved  $\text{O}_2$  by photoexcited electrons, consequently leading to generation of  $\text{OH}^\bullet$  and  $^\bullet\text{O}_2$ , respectively [17–19].

Titanium oxide ( $\text{TiO}_2$ ) is currently most applied workhouse heterogeneous photocatalyst owing to its characteristics like non-toxicity, low cost, and photochemical stability [20], though the bandgap of  $\text{TiO}_2$  is too huge ( $\sim 3.2$  eV) and its photocatalytic action decreases due to recombination of produced charge carriers [21]. The spinel ferrites,  $\text{MFe}_2\text{O}_4$  ( $\text{M} = \text{Zn, Fe, Cu, Mn, Ni, Co}$ ) have recently drawn tremendous consideration in photocatalysis owing to their environmental consonance and stability as well as their facile fabrication [22,23]. A *n*-type and *p*-type semiconductors referred to as  $\text{ZnFe}_2\text{O}_4$  (ZF) and  $\text{CoFe}_2\text{O}_4$  (CF), which respectively comprise a comparatively narrow bandgap of  $\sim 1.8$  and  $1.2$  eV, has been applied in various fields, particularly photocatalysis and electronics.  $\text{ZnFe}_2\text{O}_4$  and  $\text{CoFe}_2\text{O}_4$  have been conveyed to be well-founded photocatalysts due to their low fabrication cost, high Curie temperature, flexible valence states, high coercivity, average saturation magnetization, redox stability, and high degradation potency [24–26]. Kalam et al. [26] fabricated  $\text{CoFe}_2\text{O}_4$  magnetic nanoparticles via solvothermal technique for the elimination of methylene blue (MB). It was also reported that photodegradation of MB under visible light illumination with  $\text{CoFe}_2\text{O}_4$  nanoparticles followed first-order kinetic reaction. Arimi et al. [27] conveyed preparation of  $\text{ZnFe}_2\text{O}_4$  photocatalyst via different fabrication techniques viz polymer complex, reflux, hydrothermal, and solid-state reaction for methylene blue (MB) removal. The bleaching of MB was commenced via the transfer of electrons from photo-excited MB molecules being enclosed to the surface of  $\text{ZnFe}_2\text{O}_4$  into the CB of semiconducting ferrite [28]. It is widely known that the photocatalytic activity of spinel oxides is restricted due to their deprived environmental stability, agglomeration effect, and low electrical conductivity during

photocatalytic processes [29]. The combination of  $\text{ZnFe}_2\text{O}_4$  and  $\text{CoFe}_2\text{O}_4$  with hydroxides, nitrides, metal oxides, organic complexes, and metal-free materials provides an economical and convenient approach for enhancing photodegradation efficiency of the photocatalytic system [30,31].

Graphitic carbon nitride (GCN), a  $\pi$ -conjugated and metal-free visible light-driven semiconductor photocatalyst has a great perspective for the photodegradation of carbon-based impurities present in water [1,32–35]. GCN with a bandgap of  $\sim 2.7$  eV and VB located at  $+1.6$  eV and CB positioned at  $-1.1$  eV has received abundant consideration in recent years due to non-toxic nature, better optical performance, facile fabrication techniques, high chemical and thermal stability, and low cost. Concerning to yellow color of GCN, its optical absorption lies nearby 460 nm, making it a remarkable material for utilization of renewable solar energy. The absorption range of GCN can expand via several strategies including combination with metal oxides, metal ferrites, doping, heterojunction formation, etc. [36–38]. For example, several heterojunctions based on GCN comprehending  $\text{ZnO}/\text{GCN}$ ,  $\text{BiOBr}/\text{GCN}$ ,  $\text{WO}_3/\text{GCN}$ ,  $\text{TiO}_2/\text{GCN}$ ,  $\text{SnO}_2/\text{GCN}$ , and  $\text{MFe}_2\text{O}_4/\text{GCN}$  have been exploited to proliferate the light absorption and separation of generated  $e^-h^+$  pairs [39]. Moreover, narrow bandgap bequeaths wide light response ranges certify harvesting of visible light, that is the supposition to attain enhanced photocatalytic performance [40–42]. Accordingly, it is anticipated that the combination of  $\text{CoFe}_2\text{O}_4$  or  $\text{ZnFe}_2\text{O}_4$  with GCN and formation of type-II heterojunctions can show high photocatalytic activity due to: (i) attainment of a comprehensive visible light absorption range; (ii) having an appropriate band structure and capability to form heterojunctions; (iii) increasing the separation of produced  $e^-h^+$  pairs and proliferating the photocatalytic efficiency [42,43–46]. Hassani et al. [48] fabricated  $\text{CoFe}_2\text{O}_4/\text{mesoporous GCN}$  composite for the photodegradation of malachite green (MG), methylene blue (MB), acid orange 7, and rhodamine B (Rh B). The photocatalytic performance of  $\text{CoFe}_2\text{O}_4/\text{mesoporous GCN}$  was 1.2 times more than that of bare mesoporous GCN, which was the subsequent result of electron-hole pairs separation and increased life span of charge carriers [47]. Chen et al. synthesized  $\text{GCN}/\text{ZnFe}_2\text{O}_4$  photocatalysts via a hydrothermal procedure for the removal of spiramycin using visible light radiation. It was reported that the composite photocatalyst showed better photocatalytic performance and compound exhibited the characteristics of easy recycling and good stability [48].

In view of this, we demonstrated the photocatalytic degradation of organic dyes MO and MG over  $\text{GCN}/\text{ZnFe}_2\text{O}_4/\text{NG}$  and  $\text{GCN}/\text{CoFe}_2\text{O}_4/\text{NG}$  photocatalysts fabricated via modified hydrothermal method. The fabricated photocatalysts were magnetically separated from the reaction solution. The identification of degradation fragments and reactive species during the mineralization process was also undertaken. Lastly, dye degradation mechanism was anticipated on the basis of the obtained experimental results.

## 2. Experimental

### 2.1. Chemicals

2,4,6-trichloro-1,3,5-triazine, acetonitrile, melamine, graphene oxide,  $\text{Zn}(\text{NO}_3)_2 \cdot 6\text{H}_2\text{O}$ ,  $\text{Fe}(\text{NO}_3)_3 \cdot 9\text{H}_2\text{O}$ , sodium

hydroxide (NaOH), and urea were received from commercial suppliers without additional purification. All solutions were freshly prepared with distilled water.

## 2.2. Synthesis

For the preparation of pure GCN (Fig. 1a), 2 g of 2,4,6-trichloro-1,3,5-triazine, and 1.5 g melamine were mixed in 6 mL of acetonitrile at 60°C for 48 h. The obtained solution was cooled down to room temperature. Later, the solution was centrifuged for 15 min at 3,000 rpm, immersed in distilled water and later dried in a microwave oven at 60°C for 40 min. The formed yellow product was named as GCN and designated as GCN [47,49].

For the fabrication of nitrogen-doped graphene (NG), microwave-assisted hydrothermal method was used (Fig. 1b). In the synthesis, 2 g of graphene oxide and 1.2 g of urea were mixed in 10 mL of deionized water under ultra-sonication for 2 h at room temperature. Then the solution was centrifuged for 15 min at 3,000 rpm. The attained precipitates were washed with deionized water and oven-dried at 60°C for 3 h. The obtained product was named as NG [46].

In the typical synthesis of GCN/ZnFe<sub>2</sub>O<sub>4</sub>/NG and GCN/CoFe<sub>2</sub>O<sub>4</sub>/NG photocatalysts (Fig. 2) 0.2 g of GCN powder and 0.15 g of NG powder were dispersed in 20 mL of distilled water. Then, the solution was subjected to ultra-sonication for 30 min at room temperature. In another beaker, 10 mmol of Fe(NO<sub>3</sub>)<sub>3</sub>·9H<sub>2</sub>O and 5 mmol of Zn(NO<sub>3</sub>)<sub>2</sub>·6H<sub>2</sub>O was added to 20 mL of absolute ethanol with continuous agitation for 30 min and a uniform solution was formed. The two solutions were mixed and 4 g of NaOH (1 M) was added dropwise until pH reached 10. The reaction mixture was then cooled down to ambient temperature and centrifuged for 20 min at

3,000 rpm. The precipitates were filtered, washed with deionized water, and oven-dried at 50°C for 4 h. The formed product was labeled as GCN/ZnFe<sub>2</sub>O<sub>4</sub>/NG. Likewise, a similar method was used for fabrication of GCN/CoFe<sub>2</sub>O<sub>4</sub>/NG under same reaction conditions and 5 mmol of Co(NO<sub>3</sub>)<sub>2</sub>·6H<sub>2</sub>O was added instead of Zn(NO<sub>3</sub>)<sub>2</sub>·6H<sub>2</sub>O [24,50].

## 2.3. Evaluating the photocatalytic activity

The photocatalytic activity of the fabricated photocatalysts was estimated using double-walled pyrex vessel with water circulation under visible light [7,9]. The source of visible light used was 35 W LED lamp to irradiate the catalytic suspension comprising MO/MG solution.

The decolorization of dyes was assessed using UV-vis spectrophotometer at maximum wavelength of 520 and 620 nm for MO and MG, respectively. The photocatalytic efficiency of both photocatalysts was calculated using Eq. (1):

$$\text{Degradation Efficiency (\%)} = \frac{C_0 - C}{C_0} \times 100 \quad (1)$$

where  $C$  and  $C_0$  are respectively concentration/COD of the initial and photodegraded dye in the aqueous phase.

The degradation intermediates during the mineralization were analyzed via an high-performance liquid chromatography (HPLC) instrument (Water HPLC, Austria) well-appointed with photodiode array detector and a manual injector. The liquid chromatography–mass spectrometry investigations were accomplished on FP 5022/22-Tecna G2 20 S-TWIN FEI, (USA) having great resolution data system, double aiming instrument with the electrospray ionization and the C18 column (150 mm × 2 mm) (injection volume 20 μL).

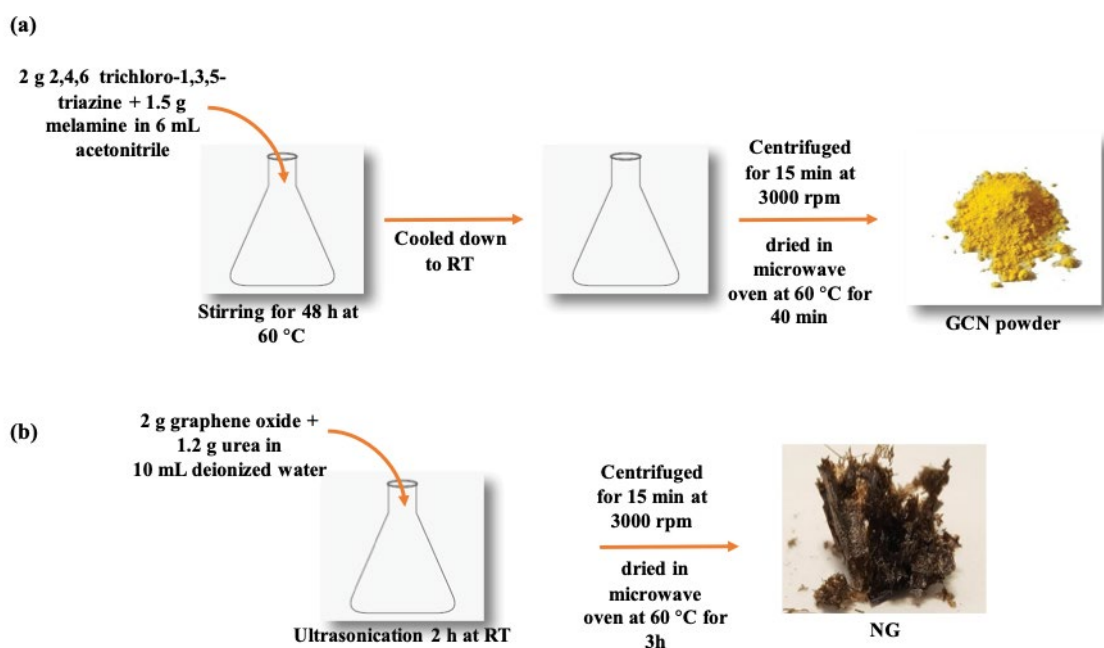


Fig. 1. Schematic illustration of (a) GCN and (b) NG synthesis using hydrothermal method.



Fig. 2. Schematic illustration of GCN/ZnFe<sub>2</sub>O<sub>4</sub>/NG synthesis. (Similar method was used for the fabrication of GCN/CoFe<sub>2</sub>O<sub>4</sub>/NG, 5 mmol of Co(NO<sub>3</sub>)<sub>2</sub>·6H<sub>2</sub>O was added instead of Zn(NO<sub>3</sub>)<sub>2</sub>·6H<sub>2</sub>O).

### 3. Results and discussion

#### 3.1. Characterization of GCN/ZnFe<sub>2</sub>O<sub>4</sub>/NG and GCN/CoFe<sub>2</sub>O<sub>4</sub>/NG heterojunctions

The internal structures of synthesized heterojunctions GCN/ZnFe<sub>2</sub>O<sub>4</sub>/NG and GCN/CoFe<sub>2</sub>O<sub>4</sub>/NG were studied by transmission electron microscopy (TEM) exhibited in Fig. 3. The TEM image of GCN/ZnFe<sub>2</sub>O<sub>4</sub>/NG displayed fine fringes of GCN, ZnFe<sub>2</sub>O<sub>4</sub> and NG. The inter-planar distance of GCN, ZnFe<sub>2</sub>O<sub>4</sub> and NG was 0.5, 0.30, and 0.4 nm, respectively recorded by high-resolution transmission electron microscopy (HRTEM). A two-dimensional wrinkled sheet-like structure observed in GCN, which was analogous to crumpled graphene, and the sheets were finely distributed on the substrate, varying from hundreds of nanometres to numerous micrometers. The morphology of ZnFe<sub>2</sub>O<sub>4</sub> was granular and ZnFe<sub>2</sub>O<sub>4</sub> nanoparticles were dispersed distinctly on GCN and NG sheets as nano-islands, which enhanced the dispersal property of layered materials and furthermore offered more photocatalytic sites [30]. The TEM and HRTEM image of GCN/CoFe<sub>2</sub>O<sub>4</sub>/NG showed fine fringes of GCN, CoFe<sub>2</sub>O<sub>4</sub> and NG and the inter-planar distance of GCN, CoFe<sub>2</sub>O<sub>4</sub> and NG was 0.5, 0.48, and 0.4 nm, respectively. The TEM image clearly concluded that CoFe<sub>2</sub>O<sub>4</sub> nanoparticles were assembled successfully on GCN and NG sheets, preserving their preliminary particle size and morphology deprived of any agglomeration [31]. These results displayed that the formation of the heterojunctions was successful.

The surface morphologies of GCN/ZnFe<sub>2</sub>O<sub>4</sub>/NG and GCN/CoFe<sub>2</sub>O<sub>4</sub>/NG heterojunctions were studied by scanning electron microscopy (SEM) as exhibited in Fig. 4. SEM images revealed that the heterojunctions consist of numerous GCN flakes loaded with CoFe<sub>2</sub>O<sub>4</sub> and ZnFe<sub>2</sub>O<sub>4</sub> nanoparticles. The porous morphology of deposited layers implies the existence of CoFe<sub>2</sub>O<sub>4</sub> and ZnFe<sub>2</sub>O<sub>4</sub> nanoparticles and well exfoliated GCN nanosheets. The GCN/CoFe<sub>2</sub>O<sub>4</sub>/NG nanocomposite exhibited mixed morphology where CoFe<sub>2</sub>O<sub>4</sub> nanoparticles were distinctly spotted to have loaded on GCN sheets [31,33]. The SEM images of GCN/ZnFe<sub>2</sub>O<sub>4</sub>/NG revealed that the heterojunction shows well-defined mesoporous 3D network [24,30,46]. It is noted that some ZnFe<sub>2</sub>O<sub>4</sub> nanospheres are compressed within GCN sheets and prevented aggregation of particles. The TEM (Fig. 3) and SEM (Fig. 4) images reveal that NG sheets display a distinctive

wrinkled structure, resulted from thermodynamically firm bending.

The energy-dispersive X-ray spectroscopy (EDS) was used to analyze chemical and elemental compositions, and the samples were composed of C, N, O, Co, Fe, Zn as expected (Fig. 5) [6,43].

The structural description of fabricated samples was performed via X-ray diffraction method (XRD) as exhibited in Fig. 6. The XRD pattern of the NG sheet displayed diffraction peak at 25.2° correspond to {0 0 2} which specifies that the nitrogen atoms have inserted into graphite crystal lattice and resulted in an increase in distance between graphitic films [44]. Two distinct diffraction peaks indicated ZnFe<sub>2</sub>O<sub>4</sub> crystal planes at 34.80° and 61.75° correspond to {3 1 1} and {4 4 0} planes, respectively. All the peaks of ZnFe<sub>2</sub>O<sub>4</sub> assigned to the spinel like structure of ZnFe<sub>2</sub>O<sub>4</sub> [42]. XRD pattern of the CoFe<sub>2</sub>O<sub>4</sub> nanoparticle displayed intense diffraction peak at 35.94° correspond to {3 1 1} and other peaks at 18.44°, 23.03°, 63.44° correspond to {1 1 1}, {2 2 0}, {4 4 0}, respectively (JCPDS no. 22-1086) [6,33]. XRD diffraction pattern of the GCN nanoparticles revealed an intense peak at 28.19° correspond to {0 0 2}, which represents inter-planar structural packing and the other peak at 2θ = 16.0° corresponds to {1 0 0} lattice planes (JCPDS no. 87-1526) parallel to c-axis and stacking of conjugated aromatic graphite alike carbon nitride [18,50]. XRD diffraction pattern of GCN/ZnFe<sub>2</sub>O<sub>4</sub>/NG nanoparticle revealed intense diffraction peak at 35.5° corresponds to {3 1 1} and another peak at 62.40° corresponds to {4 4 0} and specified successful synthesis of heterojunction photocatalyst. XRD diffraction pattern of GCN/CoFe<sub>2</sub>O<sub>4</sub>/NG heterojunction revealed a strong diffraction peak at 29.5° corresponds to {0 0 2} and other peaks at 35.40° and 60.30° corresponds to {3 1 1} and {4 4 0}, respectively.

To determine near-surface elemental compositions, chemical compositions, and some definite alteration in valence states of GCN/ZnFe<sub>2</sub>O<sub>4</sub>/NG and GCN/CoFe<sub>2</sub>O<sub>4</sub>/NG heterojunctions, X-ray photoelectron spectroscopy (XPS) characterizations were done and the results were displayed in Fig. 7. It could be observed that there are C, O, N, Co<sup>2+</sup>, Fe<sup>3+</sup>, Zn<sup>2+</sup> on both surface of GCN/ZnFe<sub>2</sub>O<sub>4</sub>/NG and GCN/CoFe<sub>2</sub>O<sub>4</sub>/NG. The peaks at 282, 397, and 527.52 eV were ascribed to the binding energies of O (1s), N (1s), and C (1s), respectively. The N 1s spectrum showed a peak attributed to graphitic nitrogen of NG [46]. The C 1s spectrum revealed

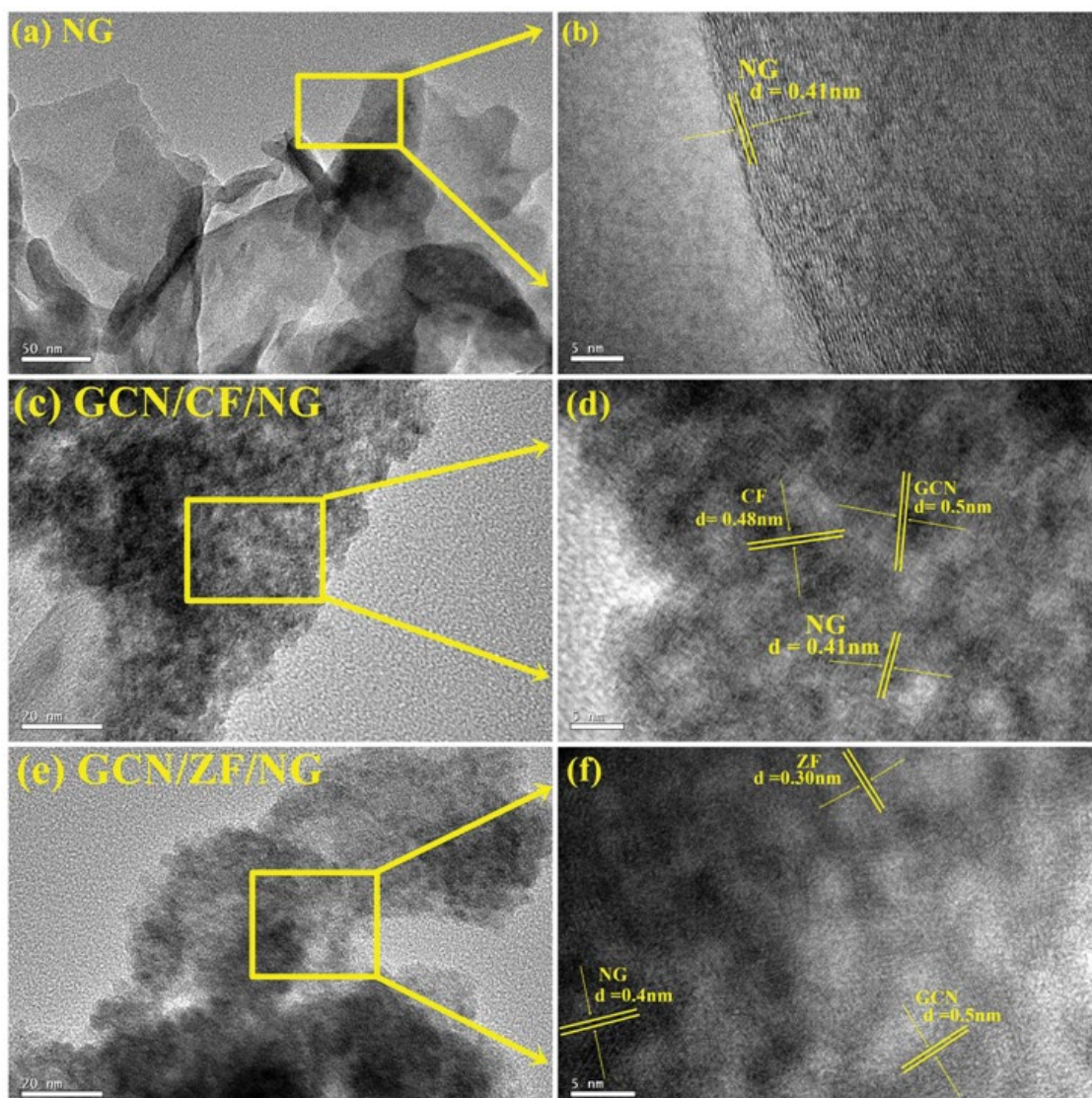


Fig. 3. TEM and HRTEM images of (a and b) pure NG, (c and d) GCN/CoFe<sub>2</sub>O<sub>4</sub>/NG, and (e and f) GCN/ZnFe<sub>2</sub>O<sub>4</sub>/NG photocatalysts.

various weak peaks corresponded to C–C sp<sup>2</sup>, C–C sp<sup>3</sup> carbon, and sp<sup>2</sup> C(N=C=N), which could be attributed to defect comprising sp<sup>2</sup> hybridized C-atoms existing in graphitic domains in the CN matrix [5]. Peaks at the binding energies of 1,019 and 1,042 eV showed an oxidation state of ZnFe<sub>2</sub>O<sub>4</sub> in 2p<sup>3</sup> are attributed to the binding energies of Zn 2p<sub>3/2</sub> and Zn 2p<sub>1/2</sub> signals in the Zn<sup>2+</sup> chemical state [42]. The spectra of Co 2p<sup>3</sup> showed two main different peaks at 793 and 770 eV attributed to Co 2p<sub>3/2</sub> and Co 2p<sub>1/2</sub>, respectively. The Fe spectra showed doublet at 722 and 708 eV, respectively allocated to Fe 2p<sub>1/2</sub> and Fe 2p<sub>3/2</sub> as satellite peaks [39,43].

The chemical functionality of NG, ZnFe<sub>2</sub>O<sub>4</sub>, CoFe<sub>2</sub>O<sub>4</sub>, GCN/ZnFe<sub>2</sub>O<sub>4</sub>/NG, and GCN/CoFe<sub>2</sub>O<sub>4</sub>/NG was further studied by FTIR analysis (Fig. S1). The FTIR spectra of GCN/ZnFe<sub>2</sub>O<sub>4</sub>/NG and GCN/CoFe<sub>2</sub>O<sub>4</sub>/NG exhibited peak around 570 cm<sup>-1</sup> attributed Zn–O and Co–O vibration, respectively. The peak around 1,480 cm<sup>-1</sup> ascribed to –OH bending and broad peak at 3,400 cm<sup>-1</sup> attributed to absorbed water molecules. Also, peak around 1,340 cm<sup>-1</sup> assigned to either C–N

or C=N stretching vibrations [23,42,51]. All these peaks assured the presence of GCN, NG, ZnFe<sub>2</sub>O<sub>4</sub> and CoFe<sub>2</sub>O<sub>4</sub> in the nanocomposite and revealed successful synthesis of both heterojunctions. The FTIR spectra of GCN presented responses of N and C heterocycles, peak at 706 cm<sup>-1</sup> accredited to triazine, and the peak in the range of 1,240–1,639 cm<sup>-1</sup> was assigned to either C–N or C=N typical stretching vibrations [42]. FTIR spectra of NG nanoparticles revealed peak 1,420 cm<sup>-1</sup> ascribed to C=C stretching. The bands positioned at 1,170 and 1,560 cm<sup>-1</sup> ascribed to νC–N and νC=C, respectively, also specified successful doping of nitrogen into graphene [44].

### 3.2. Analysis of optical properties

The optical absorption property of GCN, ZnFe<sub>2</sub>O<sub>4</sub>, and CoFe<sub>2</sub>O<sub>4</sub> nanoparticles was analyzed by UV-Vis spectroscopy. ZnFe<sub>2</sub>O<sub>4</sub>, CoFe<sub>2</sub>O<sub>4</sub>, and GCN showed strong absorption in extended UV-visible in the range 200–800 nm at 350, 450,

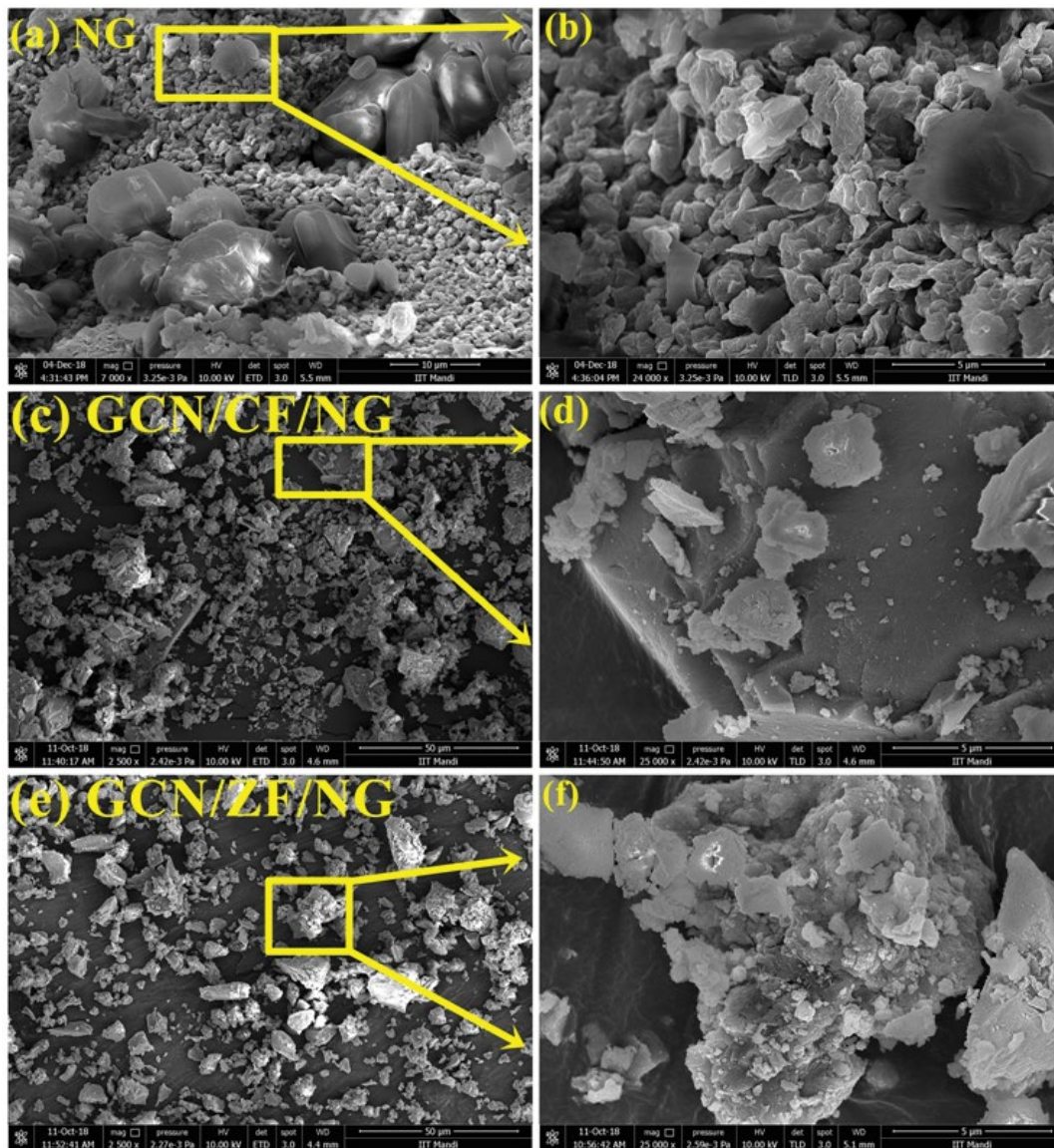


Fig. 4. SEM images of (a and b) pure NG, (c and d) GCN/CoFe<sub>2</sub>O<sub>4</sub>/NG, and (e and f) GCN/ZnFe<sub>2</sub>O<sub>4</sub>/NG photocatalysts.

and 365 nm, respectively (Fig. S2). The bandgaps of as-prepared nanoparticles were estimated by Tauc's equation  $\alpha = \alpha_0 (h\nu - E_g)^n / h\nu$  where  $\alpha$  is the absorption coefficient,  $\alpha_0$  and  $h$  are the constants and  $E_g$  is optical bandgap of the material.  $E_g$  has been illustrated by deducing linear portion of plot of  $(\alpha h\nu)^2$  against  $h\nu$ . The estimated bandgaps of GCN, GCN/CoFe<sub>2</sub>O<sub>4</sub>/NG, GCN/ZnFe<sub>2</sub>O<sub>4</sub>/NG, GCN are 2.6, 2.7, 2.4, respectively as shown in Fig. 8 [30,31,47].

### 3.3. Analysis of photoluminescence emission and Brunauer–Emmett–Teller

Photoluminescence (PL) emission were recorded to comprehend trapping, transfer and migration of electron-hole pairs. The intensity of the PL emission spectrum depends on recombination of electrons and the holes, also lower PL emission intensity, lower the recombination property of

samples [42,52]. Fig. 9(1) displayed PL spectra of the pure GCN, GCN/CoFe<sub>2</sub>O<sub>4</sub>/NG, and GCN/ZnFe<sub>2</sub>O<sub>4</sub>/NG underneath 320 nm of excitation wavelength at room temperature. It can be spotted that GCN reveal strong PL at wavelength of around 458 nm, which is corresponding to band gap of 2.7 eV. The strong PL peak of GCN attributed to band-band PL phenomenon with the energy of the light almost equal to bandgap energy of the GCN and this signal ascribed to  $n \rightarrow \pi^*$  electronic transition comprising lone pairs of N-atoms in GCN [53]. In contrast with PL of GCN, the PL emission intensities for GCN/CoFe<sub>2</sub>O<sub>4</sub>/NG and GCN/ZnFe<sub>2</sub>O<sub>4</sub>/NG was much lower, specifying that nanocomposites have minor electron-hole pairs recombination. This mainly accredited to the statement that photo-excited electrons could transfer among GCN–CoFe<sub>2</sub>O<sub>4</sub> and GCN–ZnFe<sub>2</sub>O<sub>4</sub>, so, preventing the direct electron-hole pairs recombination and enhanced the consequent photocatalytic performance of the heterojunctions.

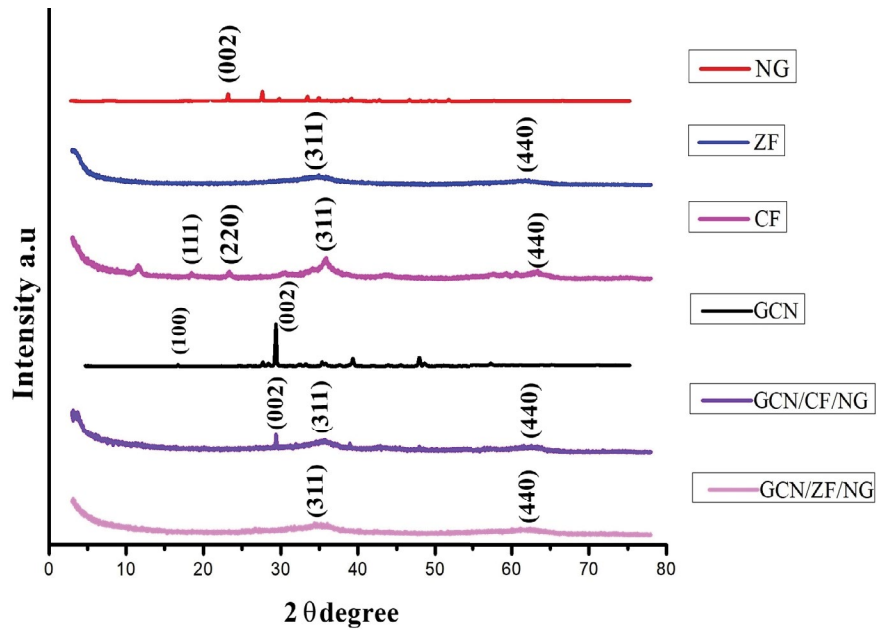


Fig. 5. XRD patterns of NG, ZnFe<sub>2</sub>O<sub>4</sub>, CoFe<sub>2</sub>O<sub>4</sub>, GCN, GCN/CoFe<sub>2</sub>O<sub>4</sub>/NG, and GCN/ZnFe<sub>2</sub>O<sub>4</sub>/NG composites.

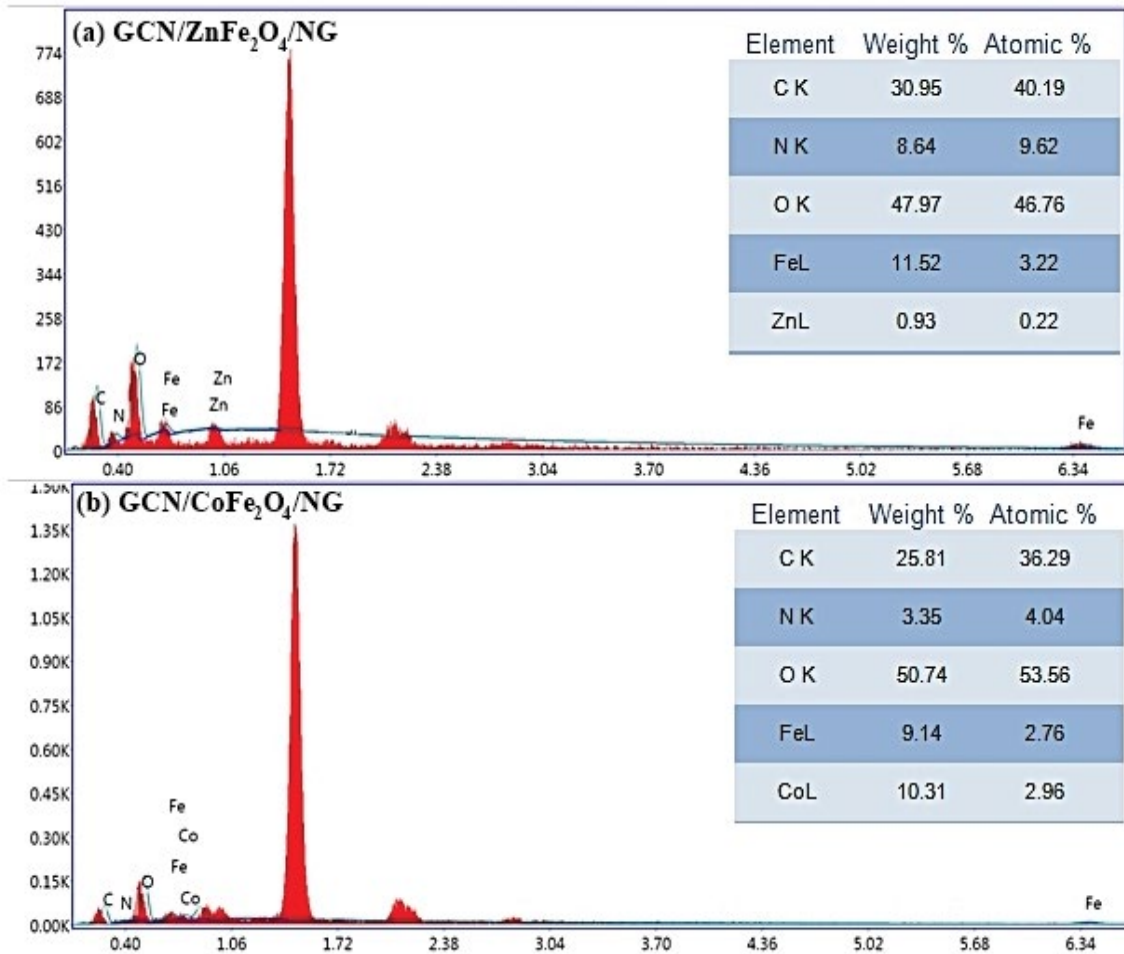


Fig. 6. EDS spectra of (a) GCN/ZnFe<sub>2</sub>O<sub>4</sub>/NG and (b) GCN/CoFe<sub>2</sub>O<sub>4</sub>/NG heterojunctions.

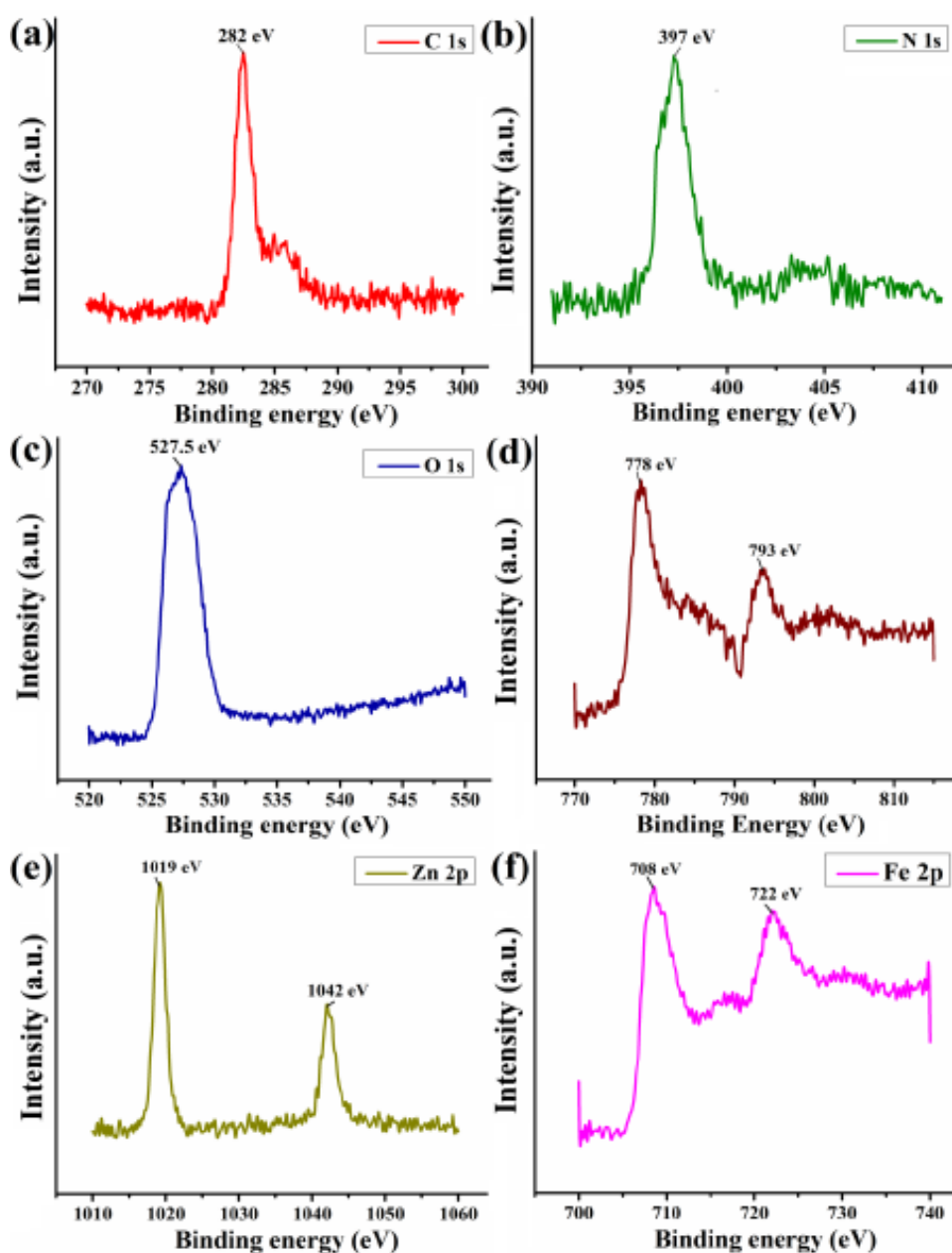


Fig. 7. XPS spectra of GCN/CoFe<sub>2</sub>O<sub>4</sub>/NG and GCN/ZnFe<sub>2</sub>O<sub>4</sub>/NG heterojunctions. Spectra of (a) C 1s, (b) N 1s, (c) O 1s, (d) Co 2p<sup>3</sup>, (e) Zn 2p<sup>3</sup>, and (f) Fe 2p<sup>3</sup>.

The Brunauer–Emmett–Teller (BET) displayed in Fig. 9 (2 and 3) explained nitrogen adsorption–desorption isotherms at 77 K and aids as a significant analysis method for the evaluation of specific surface area of the materials [54,55]. The BET detailed surface area of GCN/CoFe<sub>2</sub>O<sub>4</sub>/NG and GCN/ZnFe<sub>2</sub>O<sub>4</sub>/NG was estimated as 230 and 155 m<sup>2</sup> g<sup>-1</sup>, respectively. The addition of CoFe<sub>2</sub>O<sub>4</sub> and ZnFe<sub>2</sub>O<sub>4</sub> to GCN/NG increased the surface area of the composites and was useful for the adsorption combined photocatalytic activity of the heterojunctions.

#### 3.4. Magnetic separation of GCN/ZnFe<sub>2</sub>O<sub>4</sub>/NG and GCN/CoFe<sub>2</sub>O<sub>4</sub>/NG

The rapid separation and the recyclability of photocatalysts are essential for the efficient heterogeneous photocatalysis [31,47,56]. The magnetization hysteresis loop (M–H curve) were recorded at room temperature and exhibited in Fig. 10. GCN/ZnFe<sub>2</sub>O<sub>4</sub>/NG exhibited superparamagnetic behavior and separated from reaction solution in 20 s by employing an external permanent magnet. The saturation

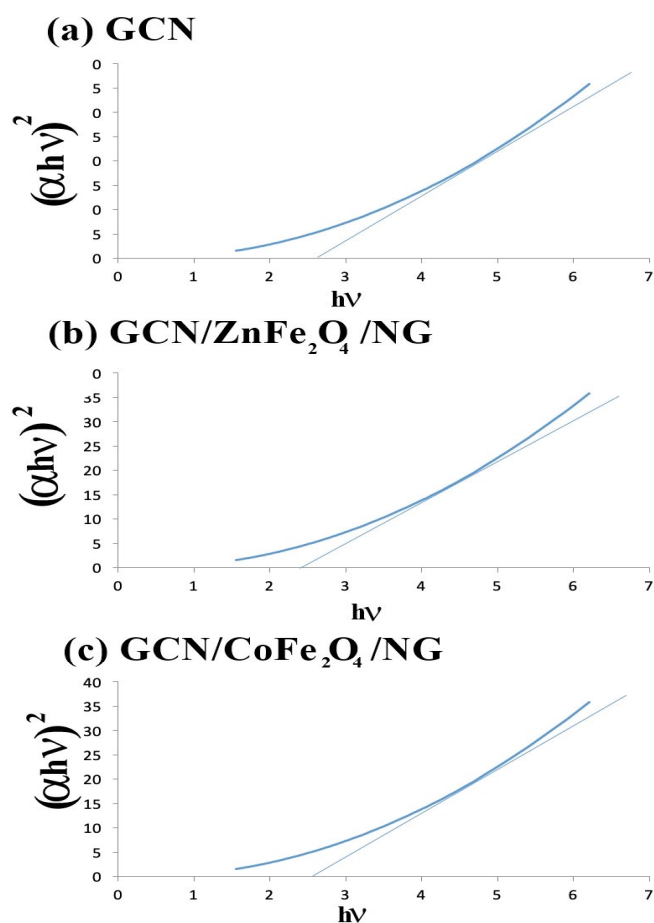


Fig. 8. Resultant Tauc plots of  $(\alpha h\nu)^2$  vs.  $h\nu$  for bandgap determination of (a) GCN, (b) GCN/ZnFe<sub>2</sub>O<sub>4</sub>/NG, and (c) GCN/CoFe<sub>2</sub>O<sub>4</sub>/NG.

magnetization ( $M_s$ ) for GCN/ZnFe<sub>2</sub>O<sub>4</sub>/NG was obtained to be 56 emu g<sup>-1</sup> and coercivity ( $H_c$ ) was zero, whereas  $M_s$  for GCN/CoFe<sub>2</sub>O<sub>4</sub>/NG was found to be 34 emu g<sup>-1</sup> and  $H_c$  of approximately 12,580 Oe. GCN/CoFe<sub>2</sub>O<sub>4</sub>/NG was separated from reaction mixture in 2 min by placing a permanent magnet.

### 3.5. Photocatalytic activity of the as-prepared photocatalysts

The photocatalytic activity and adsorption ability of MG and MO over fabricated photocatalysts were estimated. Fig. 11 reveals the elimination results of MG and MO under visible light radiation [7,19,56]. Both GCN/ZnFe<sub>2</sub>O<sub>4</sub>/NG and GCN/CoFe<sub>2</sub>O<sub>4</sub>/NG photocatalysts exhibit substantial photocatalytic activity for the removal of MG and MO dye. The photodegradation of MG after 70 min obeyed the trend: GCN/CoFe<sub>2</sub>O<sub>4</sub>/NG (98%) > GCN/ZnFe<sub>2</sub>O<sub>4</sub>/NG (93%) > CoFe<sub>2</sub>O<sub>4</sub> (50%) > ZnFe<sub>2</sub>O<sub>4</sub> (48%) > GCN (46%) > NG (28%). For MO, elimination efficiency followed the order after 140 min of photocatalytic degradation: GCN/CoFe<sub>2</sub>O<sub>4</sub>/NG (99%) > GCN/ZnFe<sub>2</sub>O<sub>4</sub>/NG (96%) > CoFe<sub>2</sub>O<sub>4</sub> (51%) > ZnFe<sub>2</sub>O<sub>4</sub> (49%) > GCN (48%) > NG (28%). Both GCN/CoFe<sub>2</sub>O<sub>4</sub>/NG and GCN/ZnFe<sub>2</sub>O<sub>4</sub>/NG were the utmost competent photocatalysts for the degradation of MO and MG, while photolysis in

the absence of photocatalysts verified that the selected dyes are stable under visible light.

### 3.6. Effect of adsorption under solar light-driven degradation of MO and MG

The adsorption experiments displayed the outcome of adsorption on the removal of MO and MG. GCN/ZnFe<sub>2</sub>O<sub>4</sub>/NG, GCN/CoFe<sub>2</sub>O<sub>4</sub>/NG, and NG showed important adsorption capability for MG and MO elimination, whereas ZnFe<sub>2</sub>O<sub>4</sub>, CoFe<sub>2</sub>O<sub>4</sub>, and GCN showed photodegradation efficiency less than 13%. Consequently, the pairing of NG with GCN/ZnFe<sub>2</sub>O<sub>4</sub> and GCN/CoFe<sub>2</sub>O<sub>4</sub> resulted in the enhanced adsorption capacity of both the photocatalyst. The pseudo-first-order (Eq. (2)) and second-order (Eq. (3) and (4)) rate expressions are explained as:

$$(q_e - q_t) = \log q_e - \frac{k_1 t}{2.303} \quad (2)$$

where  $q_t$  and  $q_e$  are respectively the amounts of dye adsorbed per gram of the adsorbent at time  $t$  and equilibrium time and  $k_1$  is the pseudo-first-order rate constant (min<sup>-1</sup>). The value of  $k_1$  and  $q_e$  can be estimated by plotting  $\log(q_e - q_t)$  vs.  $t$  [7,9].

$$\frac{q_t}{d_t} = k_2 (q_e - q_t)^2 \quad (3)$$

$$\frac{t}{q_t} = \frac{1}{k_1 q_e^2} + \frac{t}{q_t} \quad (4)$$

where  $q_t$  (mg/g) is the dye amount adsorbed at contact time " $t$ ,"  $q_e$  (mg/g) is amount of dye adsorbed per gram of adsorbent at the equilibrium and  $k_2$  (g/mg min) is second-order reaction rate constant [7,31,42]. Table S1 shows kinetic details for MO and MG adsorption on various adsorbents. The MG and MO adsorption onto GCN/ZnFe<sub>2</sub>O<sub>4</sub>/NG and GCN/CoFe<sub>2</sub>O<sub>4</sub>/NG surfaces followed the pseudo-second-order kinetic. GCN/CoFe<sub>2</sub>O<sub>4</sub>/NG, GCN/ZnFe<sub>2</sub>O<sub>4</sub>/NG, and NG, respectively, showed adsorption capability of 65.13, 66.00, and 60.00 mg/g for MG. Also, respectively 63.30, 64.29, and 60.00 mg/g of MO were adsorbed on GCN/CoFe<sub>2</sub>O<sub>4</sub>/NG, GCN/ZnFe<sub>2</sub>O<sub>4</sub>/NG, and NG. The adsorption procedure basically includes chemical adsorption comprising valence forces via exchanging or sharing of electrons amongst adsorbent and dye molecule.

The pH of solution has a vital influence to photocatalysis because wastewater is possible to be either acidic or basic [3,57,58]. Also, the reaction solution pH shows a vital role during the adsorption process and the photocatalysis of dyes on the catalyst surface. The pH was altered from 4 to 9 and the maximum MG adsorption occurred at pH 8–9, whereas maximum MO adsorption was at pH 4 (Table S2). Additionally, zeta potential study was exploited to spot the pH of zero-point charge ( $\text{pH}_{zpc}$ ). The  $\text{pH}_{zpc}$  of GCN/CoFe<sub>2</sub>O<sub>4</sub>/NG, GCN/ZnFe<sub>2</sub>O<sub>4</sub>/NG, and NG was spotted to be 6.7, 6.9, and 7.2, respectively (Fig. S3). Above  $\text{pH}_{zpc}$ , the surface of adsorbent is charged negatively and accelerates the adsorption of the cationic dye MG; while below  $\text{pH}_{zpc}$ , the surface of

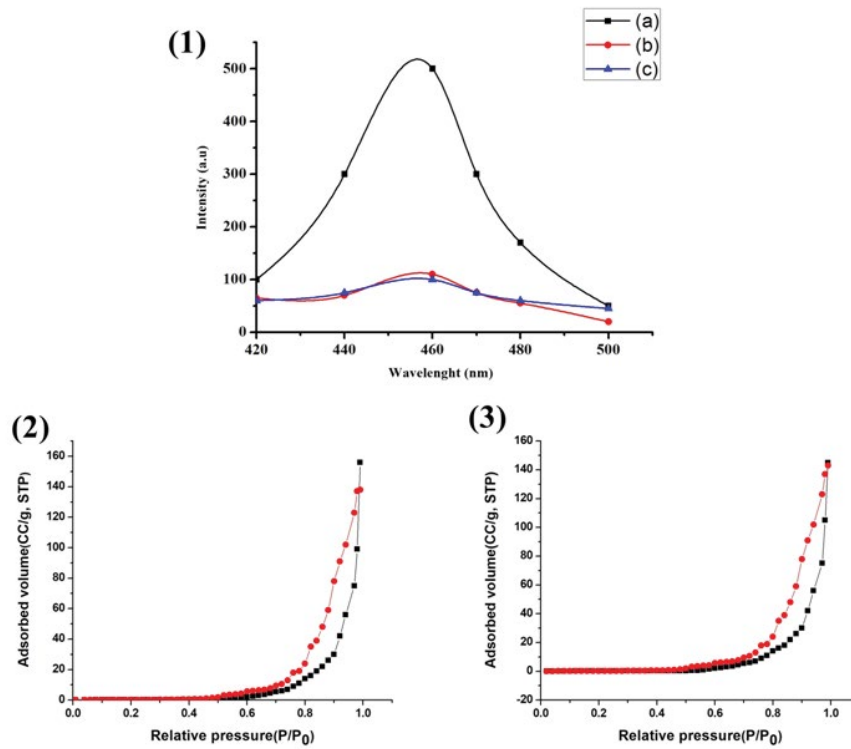


Fig. 9. (1) PL spectra of (a) GCN, (b) GCN/CoFe<sub>2</sub>O<sub>4</sub>/NG, and (c) GCN/ZnFe<sub>2</sub>O<sub>4</sub>/NG. BET isotherm for (2) GCN/ZnFe<sub>2</sub>O<sub>4</sub>/NG and (3) GCN/CoFe<sub>2</sub>O<sub>4</sub>/NG heterojunctions.

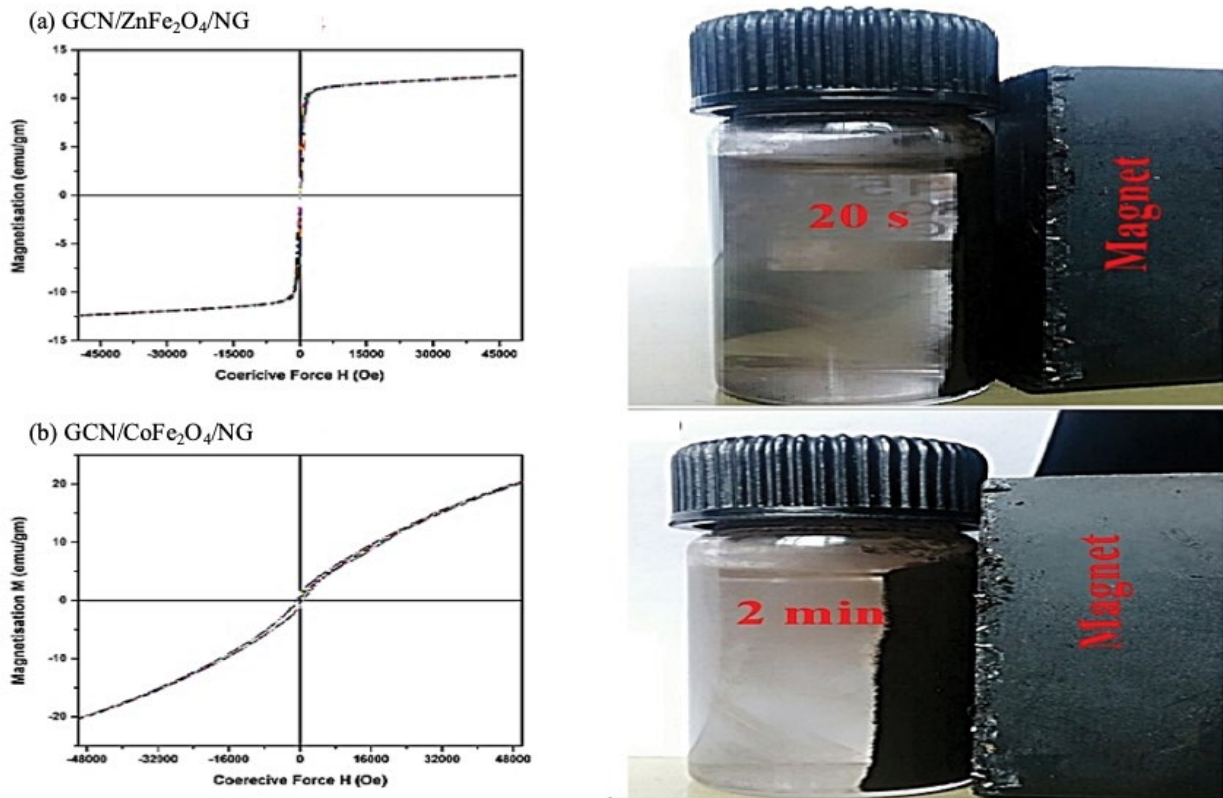


Fig. 10. Hysteresis curves of the (a) GCN/ZnFe<sub>2</sub>O<sub>4</sub>/NG and (b) GCN/CoFe<sub>2</sub>O<sub>4</sub>/NG heterojunctions and quick magnetic separation.

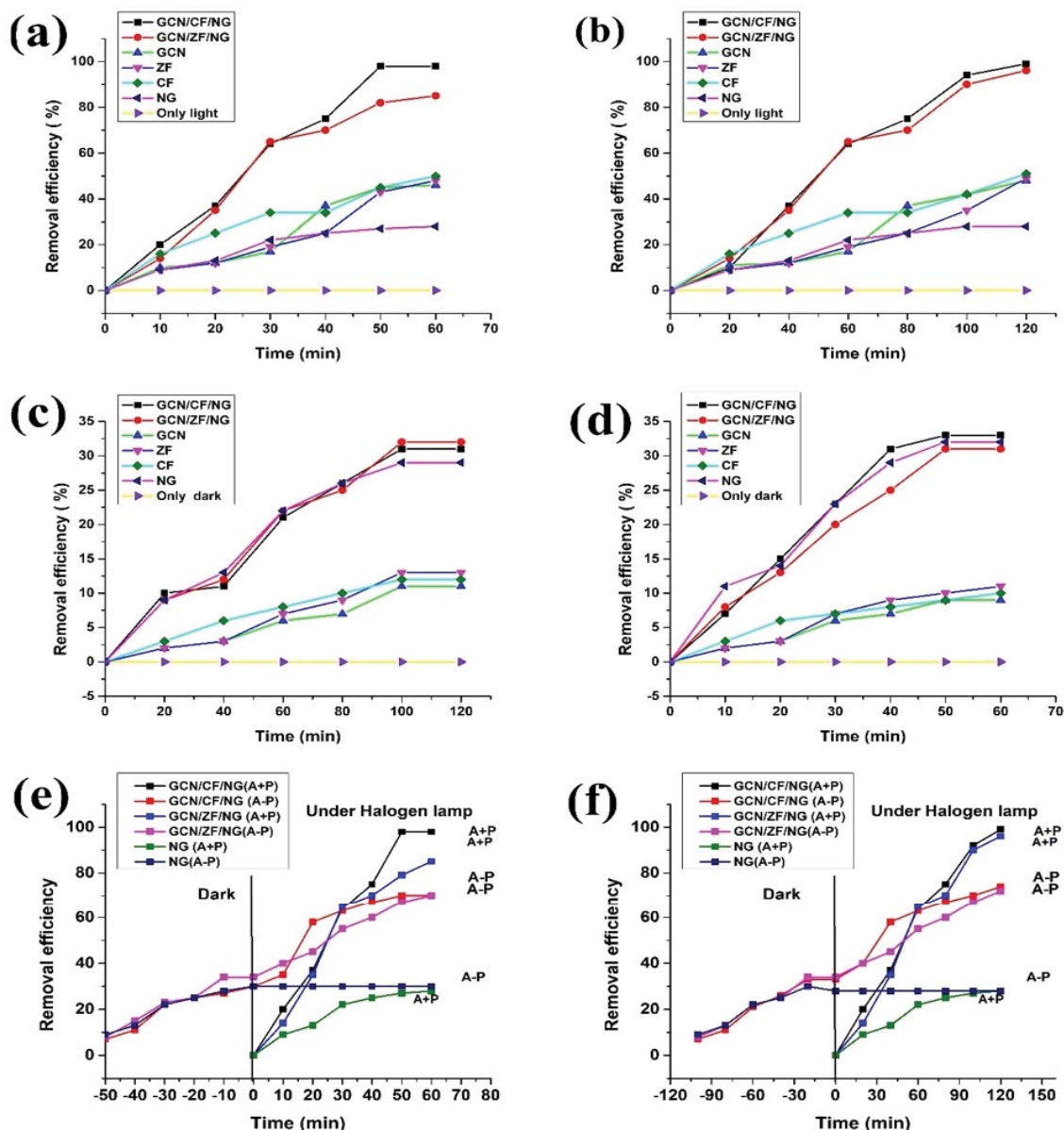


Fig. 11. Photocatalytic degradation of MO and MG over GCN/ZnFe<sub>2</sub>O<sub>4</sub>/NG and GCN/CoFe<sub>2</sub>O<sub>4</sub>/NG heterojunctions. Reaction conditions: [MO] = 1.5 × 10<sup>-5</sup> mol dm<sup>-3</sup>; [MG] = 1 × 10<sup>-5</sup> mol dm<sup>-3</sup>; [catalyst] = 50 mg/100 mL; pH = 4.0 (MO); 6 (MG); reaction time = 70 min (MG), and 140 min (MO).

adsorbent is charged positively and enables the adsorption of anionic dye MO.

Furthermore, to study the function of adsorption during the photodegradation of MO and MG using GCN/CoFe<sub>2</sub>O<sub>4</sub>/NG and GCN/ZnFe<sub>2</sub>O<sub>4</sub>/NG, the process was conducted under various reaction situations: (i) adsorption in the dark (DA); (ii) adsorption at equilibrium followed *via* photocatalysis (A–P); (iii) concurrent adsorption and photocatalysis (A+P) [57,59]. The A+P processes are more effective for photodegradation of the dyes. Through A–P route, extreme sorption of the dyes molecules on the surface of photocatalysts worked as a barrier for the visible light and deduced the inclusive photocatalytic activity. However, in the A+P processes, the adsorbed dyes molecules were

instantaneously photodegraded through catalysts beneath the illumination of halogen lamp. GCN/ZnFe<sub>2</sub>O<sub>4</sub>/NG/A+P and GCN/CoFe<sub>2</sub>O<sub>4</sub>/NG/A+P were effective for the photodegradation of MO and MG. Langmuir–Hinshelwood equation was used to explain kinetics of MG and MO elimination (Eq. (5)):

$$-\frac{dC}{dt} = kt \tag{5}$$

where  $k$  is the reaction rate coefficient and  $C$  is the concentration of dyes at time  $t$ . Integrating the above Eq. (4) (limits 0,  $C_0$ ) gives (Eq. (6)):

$$-\ln \frac{C}{C_0} = kt \quad (6)$$

The linear plot of  $-\ln(C/C_0)$  vs.  $t$  designates pseudo-first-order photodegradation process of MG and MO [57,59]. The rate constants of 0.032 and 0.034  $\text{min}^{-1}$  were attained for the MG mineralization utilizing GCN/ZnFe<sub>2</sub>O<sub>4</sub>/NG ( $R^2 = 0.98$ ) and GCN/CoFe<sub>2</sub>O<sub>4</sub>/NG ( $R^2 = 0.99$ ) photocatalysts, respectively; whilst for MO photodegradation, GCN/ZnFe<sub>2</sub>O<sub>4</sub>/NG ( $R^2 = 0.98$ ) and GCN/CoFe<sub>2</sub>O<sub>4</sub>/NG ( $R^2 = 0.97$ ) had, respectively, rate constants equal to 0.029 and 0.026  $\text{min}^{-1}$  (Table S3). The photocatalytic degradation of dyes includes both decolorization and the breakage of organic molecules into simpler inorganic molecules. In order to approve the breakage of aromatic compounds into simpler molecules, the COD removal test was done. During MG degradation process using GCN/CoFe<sub>2</sub>O<sub>4</sub>/NG and GCN/ZnFe<sub>2</sub>O<sub>4</sub>/NG, 100% of COD was eliminated within 200 min, whilst for MO degradation GCN/CoFe<sub>2</sub>O<sub>4</sub>/NG and GCN/ZnFe<sub>2</sub>O<sub>4</sub>/NG showed 100% of particular COD removal after 120 min (Figs. 10a and b).

### 3.7. Identifying degradation fragments and intermediated during MO and MG mineralization processes

In command to check the overall photodegradation of MG and MO, both dyes were subjected to photocatalysis (A+P) with respect to time. The severe decline in the absorption bands was spotted for both MG (670 nm) and MO (475 nm) with respect to time. The decrease in the absorption peaks specified decolorization on particular dyes (Figs. 12c and d).

Furthermore, in the HPLC study, peaks observed at retention times of 8 and 7 min, respectively, for MO and MG dyes. During the early degradation time, a group of peaks shown amid retention time 2–4 min and ultimately extinct after 120 min (Figs. 12e and f). This implied generation of an intermediate in the degradation procedure.

The GC–MS evaluation was also executed for MO and MG photodegradation below visible light radiation (Fig. S4). In the MG degradation process, various fragments were detected at  $m/z$  ratios of 332 (A), 211 (B), 227 (C), 122 (D), and 138 (E). During the former step of degradation process, chlorine (Cl) was removed from the MG dye to generate fragment with  $m/z$ , 316. The attack of hydroxyl radical ( $\cdot\text{OH}$ ) proceeded the demethylation with the generation of fragment A ( $m/z$ , 332). The demethylation and the attack of  $\cdot\text{OH}$  on the central C-atom resulted in emergence of two fragments with  $m/z$  ratios of 302 and 332. Further, fragment B, C and D were produced by demethylation, oxidation, and nitration processes and finally, the fragments were mineralised into H<sub>2</sub>O and CO<sub>2</sub>. The acquired degradation fragments were analogous with the earlier reported work by various researchers. The GC–MS study of degraded MO dye showed F, G, H, and I fragment with respective  $m/z$  ratios of 320, 306, 322, and 308, where fragment F was generated via MO demethylation. During the process of photocatalysis, the  $\cdot\text{OH}$  attack caused the formation of fragments G, H, and I and these fragments were consequently mineralised into H<sub>2</sub>O and CO<sub>2</sub>.

### 3.8. Detection of main reactive species during photodegradation of dyes

As demonstrated from previous conveyed work, photodegradation of dyes was generally because of the existence of oxidative species such as holes ( $h_{\text{VB}}^+$ ), electrons ( $e_{\text{CB}}^-$ ), hydroxyl radicals ( $\cdot\text{OH}$ ) and superoxide radicals ( $\cdot\text{O}_2^-$ ) [7,9]. In current work, isopropyl alcohol (IPA), chromium(VI) ion, benzoquinone (BZQ), and ammonium oxalate (AO) were exploited as trapping agent for ( $h_{\text{VB}}^+$ ), ( $e_{\text{CB}}^-$ ),  $\cdot\text{OH}$  and  $\cdot\text{O}_2^-$  scavenger, respectively. During the scavenging experiment (Fig. 13) for GCN/ZnFe<sub>2</sub>O<sub>4</sub>/NG and GCN/CoFe<sub>2</sub>O<sub>4</sub>/NG, the removal efficiency for MO after 130 min and MG after 60 min was decreased to 14% and 15%, respectively adding BZQ and IPA to the reaction mixture. In case of GCN/CoFe<sub>2</sub>O<sub>4</sub>/NG, MO and MG removal efficiency was 17% and 18% with addition of BZQ and IPA scavengers, respectively. Also, Cr(VI) and AO showed no consequence on the photodegradation of MG and MO under the halogen lamp radiation. The scavenging experiments during photocatalysis approved the existence of  $\cdot\text{OH}$  and  $\cdot\text{O}_2^-$  as chief oxygen species in MG and MO photodegradation.

### 3.9. Reusability of the heterojunctions in the photodegradation of MO and MG

The consecutive usage of the photocatalysts and also perpetuation of its photocatalytic performance display significant role for the prolonged use of photocatalyst in wide scale purpose [31,56]. During the recycle experimentations (Fig. 14), both photocatalysts were showed substantial recycle efficiency in consecutive 10 photocatalytic cycles. In every individual run, the nanocomposites were recovered magnetically using magnet, then washed with distilled water, dried, and again used for the another trial. After 10 continuous cycles, GCN/ZnFe<sub>2</sub>O<sub>4</sub>/NG displayed 98% degradation efficiency for MG and MO removal, whilst GCN/CoFe<sub>2</sub>O<sub>4</sub>/NG showed removal efficiency of 96% and 98% for the MG and MO elimination, respectively. The results noticeably revealed that composites were magnetically separable and having a great durability in the mineralization of the dyes.

## 4. Photocatalytic mechanism

### 4.1. Type-II mechanism for GCN/ZnFe<sub>2</sub>O<sub>4</sub>/NG heterojunction photocatalyst

As we are aware of the fact that efficient separation of electrons-holes at junction interfaces can remarkably enhance photocatalytic functioning of heterojunction photocatalyst [19,48,60,61]. Fig. 15a demonstrates the electron transfer mechanism in photocatalytic deterioration of malachite green and methyl orange over GCN/ZnFe<sub>2</sub>O<sub>4</sub>/NG heterojunction. Underneath visible light radiation, both ZnFe<sub>2</sub>O<sub>4</sub> and GCN are excited, the generated electrons and holes are in their CB and VB, respectively. For ZnFe<sub>2</sub>O<sub>4</sub>, the CB and VB were persistent at  $-1.2$  and  $+0.2$  eV, while CB and VB of GCN were at  $-1.26$  and  $+1.44$  eV, respectively. The CB potential of GCN is more negative than reduction potential of  $E^\circ$  ( $\text{O}_2/\cdot\text{O}_2^- = 0.33$  eV) and the VB potential of ZnFe<sub>2</sub>O<sub>4</sub> more positive than oxidation potential of

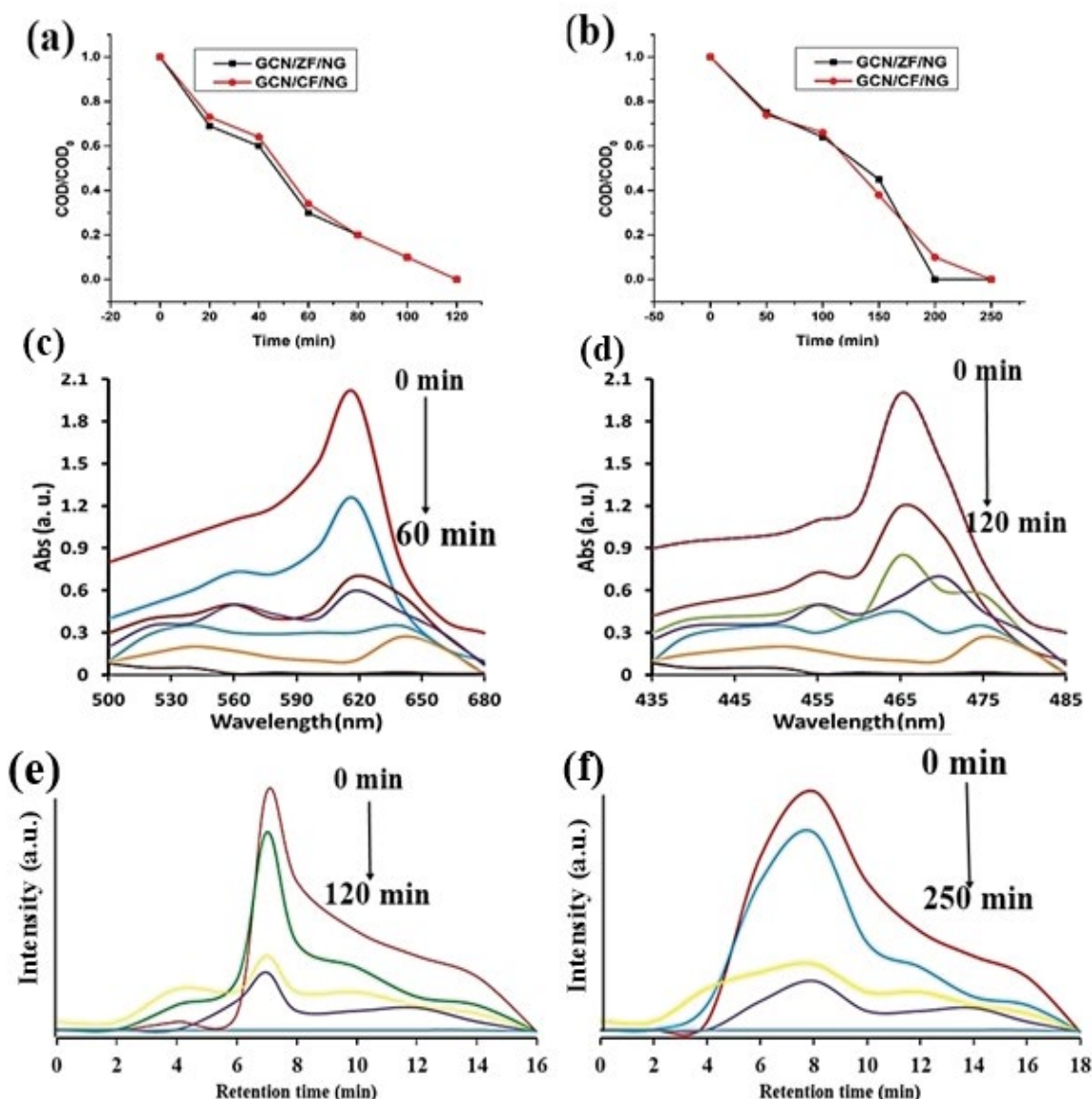


Fig. 12. COD removal during (a) MO and (b) MG mineralization. UV-visible spectra of (c) MG and (d) MO during degradation process. HPLC profile of (e) MG and (f) MO during mineralization process. Reaction conditions:  $[MO] = 1.5 \times 10^{-5} \text{ mol dm}^{-3}$ ;  $[MG] = 1 \times 10^{-5} \text{ mol dm}^{-3}$ ; [catalyst] = 50 mg/100 mL; pH = 4.0(MO); 6 (MG).

( $\cdot\text{OH}/\text{H}_2\text{O} = 2.27 \text{ eV}$ ) [62,63]. Consequently, the generated electrons in  $\text{ZnFe}_2\text{O}_4$  could transfer to surface of GCN because CB of  $\text{ZnFe}_2\text{O}_4$  is lesser than that of GCN and at the very same time, the photogenerated holes in the VB of GCN could relocate to  $\text{ZnFe}_2\text{O}_4$  surface. This route could admirably decrease the recombination of charge carriers and boost separation of generated  $e^-h^+$  pairs. Here, NG acted as electron sinker, that is, electron transporter and collector, responsible for better photocatalytic activity of the heterojunction. Also, the greater surface area of NG provided more active spots for absorption of visible light energy. The migrated electrons could react with heterojunction surface to produce excellent reactive oxygen species  $\cdot\text{O}_2^-$  which further combines with  $\text{H}^+$  from  $\text{H}_2\text{O}$  to yield  $\text{H}_2\text{O}_2$  under visible light radiation. Then to generate active  $\cdot\text{OH}$ ,

the holes could also react with the surface adsorbed  $\text{H}_2\text{O}$  or oxidize the adsorbed MO and MG molecules [60,64].

#### 4.2. Type-II mechanism for GCN/ $\text{CoFe}_2\text{O}_4$ /NG heterojunction photocatalyst

The combination of GCN and  $\text{CoFe}_2\text{O}_4$  could improve visible light captivation and stimulate  $e^-h^+$  pairs separation. The schematic representation of MG and MO degradation mechanism under visible light radiation, shown in Fig. 15b. The CB and VB of  $\text{CoFe}_2\text{O}_4$  were existed at +0.14 and +1.9 eV, while CB and VB of GCN were at -1.26 and +1.44 eV, respectively [65,66]. As CB of  $\text{CoFe}_2\text{O}_4$  is greater than that of redox potential of  $\text{O}_2/\cdot\text{O}_2^- = -0.33 \text{ eV}$ , so  $\text{O}_2$  on the heterojunction surface won't be reduced, subsequently the excited electrons

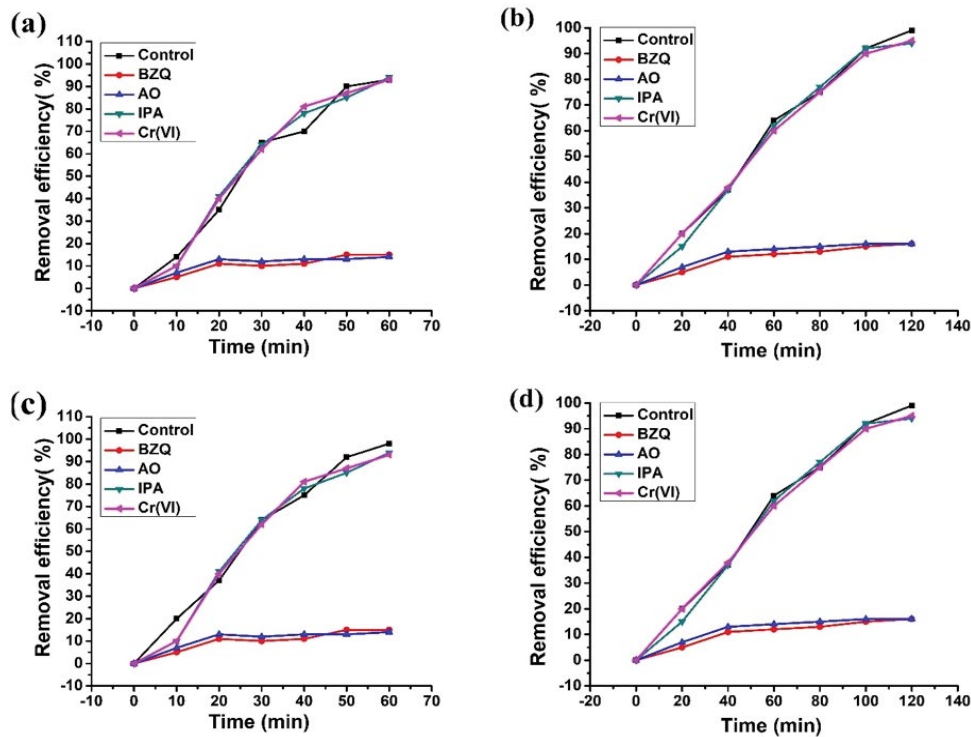


Fig. 13. Effect of various scavengers on the photodegradation of MG and MO degradation in the presence of (a and b) GCN/ZnFe<sub>2</sub>O<sub>4</sub>/NG and (c and d) GCN/CoFe<sub>2</sub>O<sub>4</sub>/NG composites. Reaction conditions: [MO] = 1.5 × 10<sup>-5</sup> mol dm<sup>-3</sup>; [MG] = 1 × 10<sup>-5</sup> mol dm<sup>-3</sup>; [catalyst] = 50 mg/100 mL; pH = 4.0 (MO); 6 (MG); reaction time = 60 min (MG) and 130 min (MO), [IPA] = 1.0 × 10<sup>-5</sup> mol dm<sup>-3</sup>, [BZQ] = 2.0 × 10<sup>-5</sup> mol dm<sup>-3</sup>, [Cr(VI)] = 1.0 × 10<sup>-5</sup> mol dm<sup>-3</sup>, [AO] = 1.5 × 10<sup>-5</sup> mol dm<sup>-3</sup>.

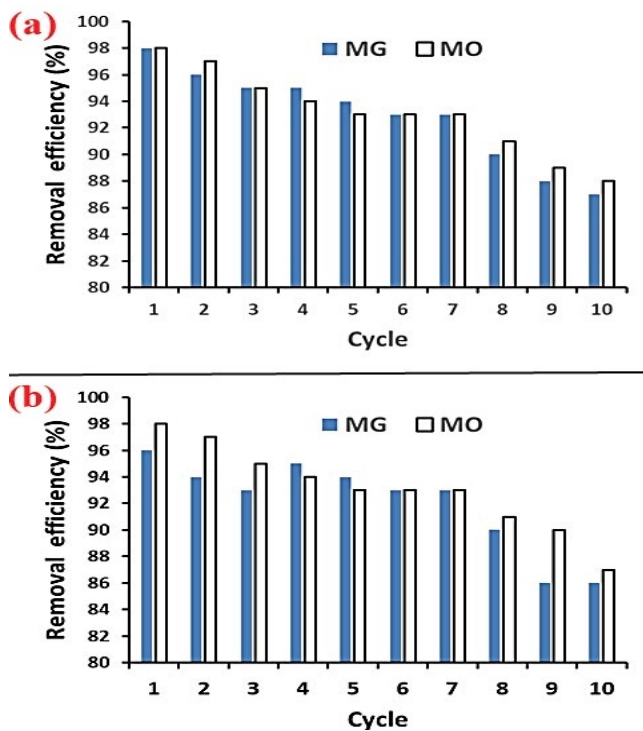


Fig. 14. (a) Recyclability of GCN/ZnFe<sub>2</sub>O<sub>4</sub>/NG and (b) GCN/CoFe<sub>2</sub>O<sub>4</sub>/NG photocatalysts in ten successive experiments for photodegradation of MO and MG under visible light irradiation.

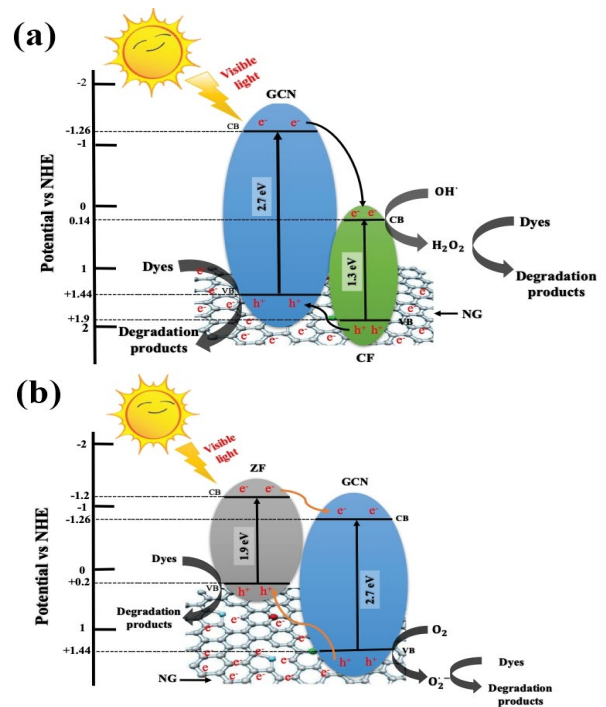


Fig. 15. Schematic mechanism of (a) GCN/CoFe<sub>2</sub>O<sub>4</sub>/NG and (b) GCN/ZnFe<sub>2</sub>O<sub>4</sub>/NG photocatalysts showing transfer of electrons and holes under visible light irradiation where NG sheet acts as electron sink.

at CB of GCN will migrate to CB of  $\text{CoFe}_2\text{O}_4$  [56,62,64]. Also, as VB of  $\text{CoFe}_2\text{O}_4$  is higher than that of VB of GCN, generated holes at VB of  $\text{CoFe}_2\text{O}_4$  will relocate to VB of GCN. Though these holes in VB of GCN cannot oxidize  $\text{OH}^-$  into  $\text{OH}\cdot$ , they can oxidize the dyes adsorbed on photocatalyst surface [47,53]. As an outcome of type-II mechanism for GCN/ $\text{CoFe}_2\text{O}_4$ /NG and GCN/ $\text{ZnFe}_2\text{O}_4$ /NG heterojunction photocatalyst,  $\cdot\text{O}_2^-$ ,  $\text{h}^+$ ,  $\cdot\text{OH}$  reacted with MO and MG molecules to mineralize into  $\text{H}_2\text{O}$  and  $\text{CO}_2$  [67–69].

## 5. Conclusion

Magnetic GCN/ $\text{CoFe}_2\text{O}_4$ /NG and GCN/ $\text{ZnFe}_2\text{O}_4$ /NG photocatalysts were successfully fabricated and efficiently used for the wastewater treatment. Structural and morphological studies of GCN/ $\text{CoFe}_2\text{O}_4$ /NG and GCN/ $\text{ZnFe}_2\text{O}_4$ /NG were investigated using TEM, SEM, XRD, XPS, and FTIR techniques. Both adsorption and photocatalytic activity of GCN/ $\text{CoFe}_2\text{O}_4$ /NG and GCN/ $\text{ZnFe}_2\text{O}_4$ /NG were spotted during MO and MG photodegradation. The MG and MO adsorption onto GCN/ $\text{ZnFe}_2\text{O}_4$ /NG and GCN/ $\text{CoFe}_2\text{O}_4$ /NG surfaces obeyed the pseudo-second-order kinetics. Also, GCN/ $\text{ZnFe}_2\text{O}_4$ /NG showed quick magnetic separation, that is, 20 s and displayed 98% degradation efficiency whereas, GCN/ $\text{CoFe}_2\text{O}_4$ /NG exhibited rapid magnetic separation, that is, 2 min and removal efficiency of 96% and 98% for MO and MG degradation, respectively. The adsorption experiments demonstrated that A+P process had synergistic effect on elimination of MG and MO, but due to extreme adsorption of dyes, A–P process hindered the degradation process. GCN/ $\text{ZnFe}_2\text{O}_4$ /NG, GCN/ $\text{CoFe}_2\text{O}_4$ /NG, and NG showed essential adsorption capability for MG and MO elimination, at the same time  $\text{ZnFe}_2\text{O}_4$ ,  $\text{CoFe}_2\text{O}_4$ , and GCN showed photodegradation efficiency less than 13%. The scavenging studies during photocatalysis verified the existence of  $\cdot\text{OH}$  and  $\cdot\text{O}_2^-$  as chief oxygen species in both MG and MO photodegradation. The magnificent photodegradation activity based on GCN/ $\text{CoFe}_2\text{O}_4$ /NG and GCN/ $\text{ZnFe}_2\text{O}_4$ /NG can be justified by following reasons: (1) type II system was founded resulted in efficient separation of electrons-holes at junction interfaces; (2) introduction of GCN onto  $\text{ZnFe}_2\text{O}_4$ /NG and  $\text{CoFe}_2\text{O}_4$ /NG surface resulted in better visible light adsorption capability. Also, recyclability of GCN/ $\text{CoFe}_2\text{O}_4$ /NG and GCN/ $\text{ZnFe}_2\text{O}_4$ /NG for ten repeated cycles displayed noticeable stability of the fabricated photocatalysts.

## References

- [1] V. Hasija, P. Raizada, A. Sudhaik, K. Sharma, A. Kumar, P. Singh, S.B. Jonnalagadda, V.K. Thakur, Recent advances in noble metal free doped graphitic carbon nitride based nanohybrids for photocatalysis of organic contaminants in water: a review, *Appl. Mater. Today*, 15 (2019) 494–524.
- [2] V. Hasija, A. Sudhaik, P. Raizada, A. Hosseini-Bandegharai, P. Singh, Carbon quantum dots supported AgI/ $\text{ZnO}$ /phosphorus doped graphitic carbon nitride as Z-scheme photocatalyst for efficient photodegradation of 2,4-dinitrophenol, *J. Environ. Chem. Eng.*, 7 (2019) 103272.
- [3] M. Pirhashemi, A. Habibi-Yangjeh, S.R. Pouran, Review on the criteria anticipated for the fabrication of highly efficient  $\text{ZnO}$ -based visible-light-driven photocatalysts, *J. Ind. Eng. Chem.*, 62 (2018) 1–25.
- [4] P. Raizada, A. Sudhaik, P. Singh, A. Hosseini-Bandegharai, P. Thakur, Converting type II AgBr/ $\text{VO}$  into ternary Z scheme photocatalyst via coupling with phosphorus doped  $\text{g-C}_3\text{N}_4$  for enhanced photocatalytic activity, *Sep. Purif. Technol.*, 12 (2019) 115692.
- [5] P. Raizada, A. Sudhaik, P. Singh, P. Shandilya, V.K. Gupta, A. Hosseini-Bandegharai, S. Agrawal,  $\text{Ag}_3\text{PO}_4$  modified phosphorus and sulphur co-doped graphitic carbon nitride as a direct Z-scheme photocatalyst for 2,4-dimethyl phenol degradation, *J. Photochem. Photobiol., A*, 374 (2019) 22–35.
- [6] D. Xiao, K. Dai, Y. Qu, Y. Yin, H. Chen, Hydrothermal synthesis of  $\alpha\text{-Fe}_2\text{O}_3/\text{g-C}_3\text{N}_4$  composite and its efficient photocatalytic reduction of Cr(VI) under visible light, *Appl. Surf. Sci.*, 358 (2015) 181–187.
- [7] A. Habibi-Yangjeh, M. Mousavi, K. Nakata, Boosting visible-light photocatalytic performance of  $\text{g-C}_3\text{N}_4/\text{Fe}_3\text{O}_4$  anchored with  $\text{CoMoO}_4$  nanoparticles: novel magnetically recoverable photocatalysts, *J. Photochem. Photobiol., A*, 368 (2019) 120–136.
- [8] A. Sudhaik, P. Raizada, P. Shandilya, P. Singh, Magnetically recoverable graphitic carbon nitride and  $\text{NiFe}_2\text{O}_4$  based magnetic photocatalyst for degradation of oxytetracycline antibiotic in simulated wastewater under solar light, *J. Environ. Chem. Eng.*, 6 (2018) 3874–3883.
- [9] K. Sharma, V. Dutta, S. Sharma, P. Raizada, A. Hosseini-Bandegharai, P. Thakur, P. Singh, Recent advances in enhanced photocatalytic activity of bismuth oxyhalides for efficient photocatalysis of organic pollutants in water: a review, *J. Ind. Eng. Chem.*, 78 (2019) 1–20.
- [10] P. Shandilya, D. Mittal, A. Sudhaik, M. Soni, P. Raizada, A.K. Saini, P. Singh,  $\text{GdVO}_4$  modified fluorine doped graphene nanosheets as dispersed photocatalyst for mitigation of phenolic compounds in aqueous environment and bacterial disinfection, *Sep. Purif. Technol.*, 210 (2019) 804–816.
- [11] A. Sudhaik, P. Raizada, P. Shandilya, D.Y. Jeong, J.H. Lim, P. Singh, Review on fabrication of graphitic carbon nitride based efficient nanocomposites for photodegradation of aqueous phase organic pollutants, *J. Ind. Eng. Chem.*, 67 (2018) 28–51.
- [12] A. Habibi-Yangjeh, M. Mousavi, Deposition of  $\text{CuWO}_4$  nanoparticles over  $\text{g-C}_3\text{N}_4/\text{Fe}_3\text{O}_4$  nanocomposite: novel magnetic photocatalysts with drastically enhanced performance under visible-light, *Adv. Powder Technol.*, 29 (2018) 1379–1392.
- [13] P. Singh, P. Shandilya, P. Raizada, A. Sudhaik, A. Rahmani-Sani, A. Hosseini-Bandegharai, Review on various strategies for enhancing photocatalytic activity of graphene based nanocomposites for water purification, *Arabian J. Chem.*, 13 (2018) 3498–3520.
- [14] S. Asadzadeh-Khaneghah, A. Habibi-Yangjeh, D. Seifzadeh, Graphitic carbon nitride nanosheets coupled with carbon dots and  $\text{BiOI}$  nanoparticles: boosting visible-light-driven photocatalytic activity, *J. Taiwan Inst. Chem. Eng.*, 87 (2018) 98–111.
- [15] P. Singh, Sonu, P. Raizada, A. Sudhaik, P. Shandilya, P. Thakur, S. Agarwal, V.K. Gupta, Enhanced photocatalytic activity and stability of AgBr/ $\text{BiOBr}$ /graphene heterojunction for phenol degradation under visible light, *J. Saudi Chem. Soc.*, 23 (2018) 586–599.
- [16] P. Singh, K. Sharma, V. Hasija, V. Sharma, S. Sharma, P. Raizada, M. Singh, A.K. Saini, A. Hosseini-Bandegharai, V.K. Thakur, Systematic review on applicability of magnetic iron oxides-integrated photocatalysts for degradation of organic pollutants in water, *Mater. Today Chem.*, 14 (2019) 100186.
- [17] N. Chandel, K. Sharma, A. Sudhaik, P. Raizada, A. Hosseini-Bandegharai, V.K. Thakur, P. Singh, Magnetically separable  $\text{ZnO}/\text{ZnFe}_2\text{O}_4$  and  $\text{ZnO}/\text{CoFe}_2\text{O}_4$  photocatalysts supported onto nitrogen doped graphene for photocatalytic degradation of toxic dyes, *Arabian J. Chem.*, 13 (2019) 4324–4340.
- [18] D. Kong, Y. Zheng, M. Kobielski, Y. Wang, Z. Bai, W. Macyk, X. Wang, J. Tang, Recent advances in visible light-driven water oxidation and reduction in suspension systems, *Mater. Today*, 21 (2018) 897–924.
- [19] L. Chen, Y. Man, Z. Chen, Y. Zhang, Ag/ $\text{g-C}_3\text{N}_4$  layered composites with enhanced visible light photocatalytic performance, *Mater. Res. Express*, 3 (2016) 115003.

- [20] S. Sharma, V. Dutta, P. Singh, P. Raizada, A. Rahmani-Sani, A. Hosseini-Bandegharai, V.K. Thakur, Carbon quantum dot supported semiconductor photocatalysts for efficient degradation of organic pollutants in water: a review, *J. Cleaner Prod.*, 228 (2019) 755–769.
- [21] M. Hadnadjev-Kostic, T. Vulic, R. Marinkovic-Neducin, D. Lončarević, J. Dostanić, S. Markov, D. Jovanović, Photo-induced properties of photocatalysts: a study on the modified structural, optical and textural properties of TiO<sub>2</sub>-ZnAl layered double hydroxide based materials, *J. Cleaner Prod.*, 164 (2017) 1–8.
- [22] R. Miao, Z. Luo, W. Zhong, S.Y. Chen, T. Jiang, B. Dutta, Y. Nasr, Y. Zhang, S.L. Suib, Mesoporous TiO<sub>2</sub> modified with carbon quantum dots as a high-performance visible light photocatalyst, *Appl. Catal., B*, 189 (2016) 26–38.
- [23] D. Cao, L. Pan, J. Li, X. Cheng, Z. Zhao, J. Xu, Q. Li, X. Wang, S. Li, J. Wang, Q. Liu, Investigation on the structures and magnetic properties of carbon or nitrogen doped cobalt ferrite nanoparticles, *Sci. Rep.*, 8 (2018) 7916.
- [24] C. Borgohain, K.K. Senapati, K.C. Sarma, P. Phukan, A facile synthesis of nanocrystalline CoFe<sub>2</sub>O<sub>4</sub> embedded one-dimensional ZnO hetero-structure and its use in photocatalysis, *J. Mol. Catal. A*, 363–364 (2012) 495–500.
- [25] B. Joshi, E. Samuel, T.G. Kim, C.W. Park, Y.I. Kim, M.T. Swihart, W.Y. Yoon, S.S. Yoon, Supersonically spray-coated zinc ferrite/graphitic-carbon nitride composite as a stable high-capacity anode material for lithium-ion batteries, *J. Alloys Compd.*, 768 (2018) 525–534.
- [26] A. Kalam, A.G. Al-Sehemi, M. Assiri, G. Du, T. Ahmad, I. Ahmad, M. Pannipara, Modified solvothermal synthesis of cobalt ferrite (CoFe<sub>2</sub>O<sub>4</sub>) magnetic nanoparticles photocatalysts for degradation of methylene blue with H<sub>2</sub>O<sub>2</sub>/visible light, *Results Phys.*, 8 (2018) 1046–1053.
- [27] A. Arimi, L. Megatiff, L.I. Granone, R. Dillert, D.W. Bahnemann, Visible-light photocatalytic activity of zinc ferrites, *J. Photochem. Photobiol., A*, 366 (2018) 118–126.
- [28] K. Maaz, A. Mumtaz, S.K. Hasanain, A. Ceylan, Synthesis and magnetic properties of cobalt ferrite (CoFe<sub>2</sub>O<sub>4</sub>) nanoparticles prepared by wet chemical route, *J. Magn. Magn. Mater.*, 308 (2007) 289–95.
- [29] K.K. Kefeni, B.B. Mamba, T.A. Msagati, Application of spinel ferrite nanoparticles in water and wastewater treatment: a review, *Sep. Purif. Technol.*, 188 (2017) 399–422.
- [30] H.J. Cui, J.W. Shi, B. Yuan, M.L. Fu, Synthesis of porous magnetic ferrite nanowires containing Mn and their application in water treatment, *J. Mater. Chem. A*, 1 (2013) 5902–5907.
- [31] P. Raizada, P. Thakur, A. Sudhaik, P. Singh, V.K. Thakur, A. Hosseini-Bandegharai, Fabrication of dual Z-scheme photocatalyst via coupling of BiOBr/Ag/AgCl heterojunction with P and S co-doped g-C<sub>3</sub>N<sub>4</sub> for efficient phenol degradation, *Arabian J. Chem.*, 13 (2020) 4538–4552.
- [32] A. Hassani, P. Eghbali, A. Ekicibil, O. Metin, Monodisperse cobalt ferrite nanoparticles assembled on mesoporous graphitic carbon nitride (CoFe<sub>2</sub>O<sub>4</sub>/mpg-C<sub>3</sub>N<sub>4</sub>): a magnetically recoverable nanocomposite for the photocatalytic degradation of organic dyes, *J. Magn. Magn. Mater.*, 456 (2018) 400–412.
- [33] L. Lu, Z. Lv, Y. Si, M. Liu, S. Zhang, Recent progress on band and surface engineering of graphitic carbon nitride for artificial photosynthesis, *Appl. Surf. Sci.*, 462 (2018) 693–712.
- [34] S. Gautam, P. Shandilya, B. Priya, V.P. Singh, P. Raizada, R. Rai, M.A. Valente, P. Singh, Superparamagnetic MnFe<sub>2</sub>O<sub>4</sub> dispersed over graphitic carbon sand composite and bentonite as magnetically recoverable photocatalyst for antibiotic mineralization, *Sep. Purif. Technol.*, 172 (2017) 498–511.
- [35] S.C. Yan, Z.S. Li, Z.G. Zou, Photodegradation performance of g-C<sub>3</sub>N<sub>4</sub> fabricated by directly heating melamine, *Langmuir*, 25 (2009) 10397–10401.
- [36] S.C. Yan, Z.S. Li, Z.G. Zou, Photodegradation of rhodamine B and methyl orange over boron-doped g-C<sub>3</sub>N<sub>4</sub> under visible light irradiation, *Langmuir*, 26 (2010) 3894–3901.
- [37] F. Dong, Z. Zhao, T. Xiong, Z. Ni, W. Zhang, Y. Sun, W.K. Ho, In situ construction of g-C<sub>3</sub>N<sub>4</sub>/g-C<sub>3</sub>N<sub>4</sub> metal-free heterojunction for enhanced visible-light photocatalysis, *ACS Appl. Mater. Interfaces*, 5 (2013) 11392–11401.
- [38] S. Asadzadeh-Khaneghah, A. Habibi-Yangjeh, K. Nakata, Decoration of carbon dots over hydrogen peroxide treated graphitic carbon nitride: exceptional photocatalytic performance in removal of different contaminants under visible light, *J. Photochem. Photobiol., A*, 374 (2019) 161–172.
- [39] M.J. Bojdys, J.O. Müller, M. Antonietti, A. Thomas, Ionothermal synthesis of crystalline, condensed, graphitic carbon nitride, *Chem. Eur. J.*, 14 (2008) 8177–8182.
- [40] A. Kumar, P. Raizada, P. Singh, R. Saini, A. Saini, A. Hosseini-Bandegharai, Perspective and status of polymeric graphitic carbon nitride based Z-scheme photocatalytic systems for sustainable photocatalytic water purification, *Chem. Eng. J.*, (2019) 123496.
- [41] J. Wen, J. Xie, X. Chen, X. Li, A review on g-C<sub>3</sub>N<sub>4</sub>-based photocatalysts, *Appl. Surf. Sci.*, 391 (2017) 72–123.
- [42] X. Bai, L. Wang, R. Zong, Y. Zhu, Photocatalytic activity enhanced via g-C<sub>3</sub>N<sub>4</sub> nanoplates to nanorods, *J. Phys. Chem. C*, 117 (2013) 9952–9961.
- [43] L. Chen, W. Ma, J. Dai, J. Zhao, C. Li, Y. Yan, Facile synthesis of highly efficient graphitic-C<sub>3</sub>N<sub>4</sub>/ZnFe<sub>2</sub>O<sub>4</sub> heterostructures enhanced visible-light photocatalysis for spiramycin degradation, *J. Photochem. Photobiol., A*, 328 (2016) 24–32.
- [44] L. Gan, S. Shang, C.W. Yuen, S.X. Jiang, E. Hu, Hydrothermal synthesis of magnetic CoFe<sub>2</sub>O<sub>4</sub>/graphene nanocomposites with improved photocatalytic activity, *Appl. Surf. Sci.*, 351 (2015) 140–147.
- [45] R. Singh, J. Ladol, H. Khajuria, H.N. Sheikh, Nitrogen doped graphene nickel ferrite magnetic photocatalyst for the visible light degradation of methylene blue, *Acta Chim. Sin.*, 64 (2017) 170–178.
- [46] T. Zhu, Y. Song, H. Ji, Y. Xu, Y. Song, J. Xia, S. Yin, Y. Li, H. Xu, Q. Zhang, H. Li, Synthesis of g-C<sub>3</sub>N<sub>4</sub>/Ag<sub>3</sub>VO<sub>4</sub> composites with enhanced photocatalytic activity under visible light irradiation, *Chem. Eng. J.*, 271 (2015) 96–105.
- [47] H. Xu, L. Ma, Z. Jin, Nitrogen-doped graphene: synthesis, characterizations and energy applications, *J. Energy Chem.*, 27 (2018) 146–160.
- [48] K. Sridharan, T. Kuriakose, R. Philip, T.J. Park, Transition metal (Fe, Co and Ni) oxide nanoparticles grafted graphitic carbon nitrides as efficient optical limiters and recyclable photocatalysts, *Appl. Surf. Sci.*, 308 (2014) 139–147.
- [49] K.K. Das, S. Patnaik, S. Mansingh, A. Behera, A. Mohanty, C. Acharya, K.M. Parida, Enhanced photocatalytic activities of polypyrrole sensitized zinc ferrite/graphitic carbon nitride n-n heterojunction towards ciprofloxacin degradation, hydrogen evolution and antibacterial studies, *J. Colloid Interface Sci.*, 561 (2020) 551–567.
- [50] Y. Cui, Y. Tang, X. Wang, Template-free synthesis of graphitic carbon nitride hollow spheres for photocatalytic degradation of organic pollutants, *Mater. Lett.*, 161 (2015) 197–200.
- [51] R. Li, M. Cai, Z. Xie, Q. Zhang, Y. Zeng, H. Liu, W. Lv, Construction of heterostructured CuFe<sub>2</sub>O<sub>4</sub>/g-C<sub>3</sub>N<sub>4</sub> nanocomposite as an efficient visible light photocatalyst with peroxydisulfate for the organic oxidation, *Appl. Catal., B*, 244 (2019) 974–982.
- [52] S. Singh, S. Singhal, Transition metal doped cobalt ferrite nanoparticles: efficient photocatalyst for photodegradation of textile dye, *Mater. Today*, 14 (2019) 453–460.
- [53] W. Wang, N. Li, K. Hong, H. Guo, R. Ding, Z. Xia, Z-scheme recyclable photocatalysts based on flower-like nickel zinc ferrite nanoparticles/ZnO nanorods: enhanced activity under UV and visible irradiation, *J. Alloys Compd.*, 777 (2019) 1108–1114.
- [54] D.R. Paul, R. Sharma, P. Panchal, S.P. Nehra, A.P. Gupta, A. Sharma, Synthesis, characterization and application of silver doped graphitic carbon nitride as photocatalyst towards visible light photocatalytic hydrogen evolution, *Int. J. Hydrogen Energy*, (2019), doi: 10.1016/j.ijhydene.2019.06.061.
- [55] K. Singh, The use of nitrogen adsorption for the characterisation of porous materials, *Colloids Surf., A*, 187 (2001) 3–9.
- [56] W. Chen, Z.C. He, G.B. Huang, C.L. Wu, W.F. Chen, X.H. Liu, Direct Z-scheme 2D/2D MnIn<sub>2</sub>S<sub>4</sub>/g-C<sub>3</sub>N<sub>4</sub> architectures with highly efficient photocatalytic activities towards treatment of pharmaceutical wastewater and hydrogen evolution, *Chem. Eng. J.*, 359 (2019) 244–253.

- [57] S. Huang, Y. Xu, M. Xie, H. Xu, M. He, J. Xia, L. Huang, H. Li, Synthesis of magnetic  $\text{CoFe}_2\text{O}_4/\text{g-C}_3\text{N}_4$  composite and its enhancement of photocatalytic ability under visible-light, *Colloids Surf., A*, 478 (2015) 71–80.
- [58] P. Singh, S. Gautam, P. Shandilya, B. Priya, V.P. Singh, P. Raizada, Graphene bentonite supported  $\text{ZnFe}_2\text{O}_4$  as superparamagnetic photocatalyst for antibiotic degradation, *Adv. Mater. Lett.*, 8 (2017) 229–238.
- [59] P. Shandilya, D. Mittal, M. Soni, P. Raizada, A. Hosseini-Bandegharai, A.K. Saini, P. Singh, Fabrication of fluorine doped graphene and  $\text{SmVO}_4$  based dispersed and adsorptive photocatalyst for abatement of phenolic compounds from water and bacterial disinfection, *J. Cleaner Prod.*, 203 (2018) 386–399.
- [60] P. Shandilya, D. Mittal, M. Soni, P. Raizada, A. Hosseini-Bandegharai, A.K. Saini, P. Singh, Fabrication of fluorine doped graphene and  $\text{SmVO}_4$  based dispersed and adsorptive photocatalyst for abatement of phenolic compounds from water and bacterial disinfection, *J. Cleaner Prod.*, 203 (2018) 386–399.
- [61] V. Dutta, P. Singh, P. Shandilya, S. Sharma, P. Raizada, A.K. Saini, V.K. Gupta, A. Hosseini-Bandegharai, S. Agarwal, A. Rahmani-Sani, Review on advances in photocatalytic water disinfection utilizing graphene and graphene derivatives-based nanocomposites, *J. Environ. Chem. Eng.*, 7 (2019) 103–132.
- [62] F.A. Harraz, R.M. Mohamed, M.M. Rashad, Y.C. Wang, W. Sigmund, Magnetic nanocomposite based on titania-silica/cobalt ferrite for photocatalytic degradation of methylene blue dye, *Ceram. Int.*, 40 (2014) 375–384.
- [63] S. Xu, D. Feng, W. Shangguan, Preparations and photocatalytic properties of visible-light-active zinc ferrite-doped  $\text{TiO}_2$  photocatalyst, *J. Phys. Chem. C.*, 113 (2019) 2463–2467.
- [64] P.P. Hankare, R.P. Patil, A.V. Jadhav, K.M. Garadkar, R. Sasikala, Enhanced photocatalytic degradation of methyl red and thymol blue using titania-alumina-zinc ferrite nanocomposite, *Appl. Catal., B*, 107 (2011) 333–339.
- [65] V. Dutta, S. Sharma, P. Raizada, A. Hosseini-Bandegharai, V.K. Gupta, P. Singh, Review on augmentation in photocatalytic activity of  $\text{CoFe}_2\text{O}_4$  via heterojunction formation for photocatalysis of organic pollutants in water, *J. Saudi Chem. Soc.*, 23 (2019) 1119–1136.
- [66] D.R. Paul, R. Sharma, S.P. Nehra, A. Sharma, Effect of calcination temperature, pH and catalyst loading on photodegradation efficiency of urea derived graphitic carbon nitride towards methylene blue dye solution, *RSC Adv.*, 9 (2019) 15381–15391.
- [67] D.R. Paul, R. Sharma, P. Panchal, R. Malik, A. Sharma, V.K. Tomer, S.P. Nehra, Silver doped graphitic carbon nitride for the enhanced photocatalytic activity towards organic dyes, *J. Nanosci. Nanotechnol.*, 19 (2019) 5241–5248.
- [68] P. Panchal, D.R. Paul, A. Sharma, D. Hooda, R. Yadav, P. Meena, S.P. Nehra, Phytoextract mediated ZnO/MgO nanocomposites for photocatalytic and antibacterial activities, *J. Photochem. Photobiol., A*, 385 (2019) 112049.
- [69] D. Patidar, A. Yadav, D.R. Paul, A. Sharma, S.P. Nehra, Nano hybrids cadmium reduced-graphene oxide for improving photo-degradation of methylene blue, *Physica E*, 114 (2019) 113560.

#### Supplementary information:

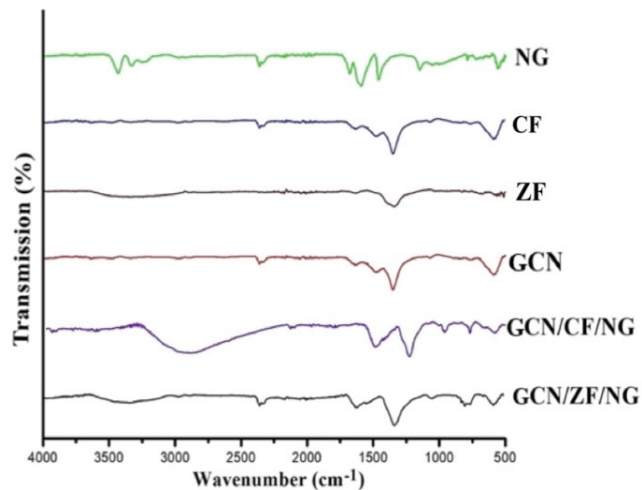


Fig. S1. FTIR spectra of NG,  $\text{ZnFe}_2\text{O}_4$ ,  $\text{CoFe}_2\text{O}_4$ , GCN, GCN/ $\text{CoFe}_2\text{O}_4$ /NG, and GCN/ $\text{ZnFe}_2\text{O}_4$ /NG photocatalysts.

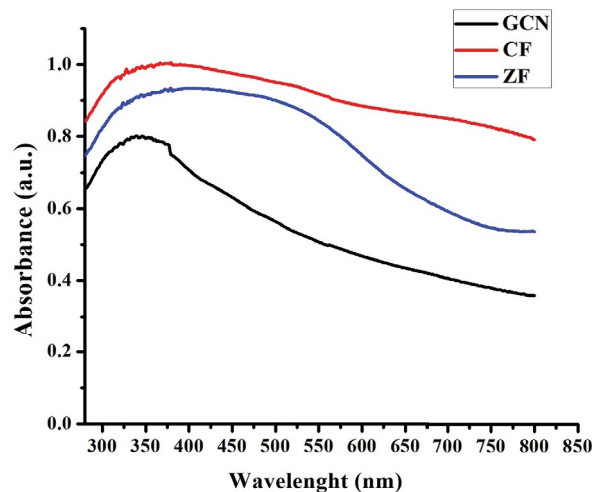


Fig. S2. UV-vis absorption spectra of  $\text{ZnFe}_2\text{O}_4$ ,  $\text{CoFe}_2\text{O}_4$  and GCN.

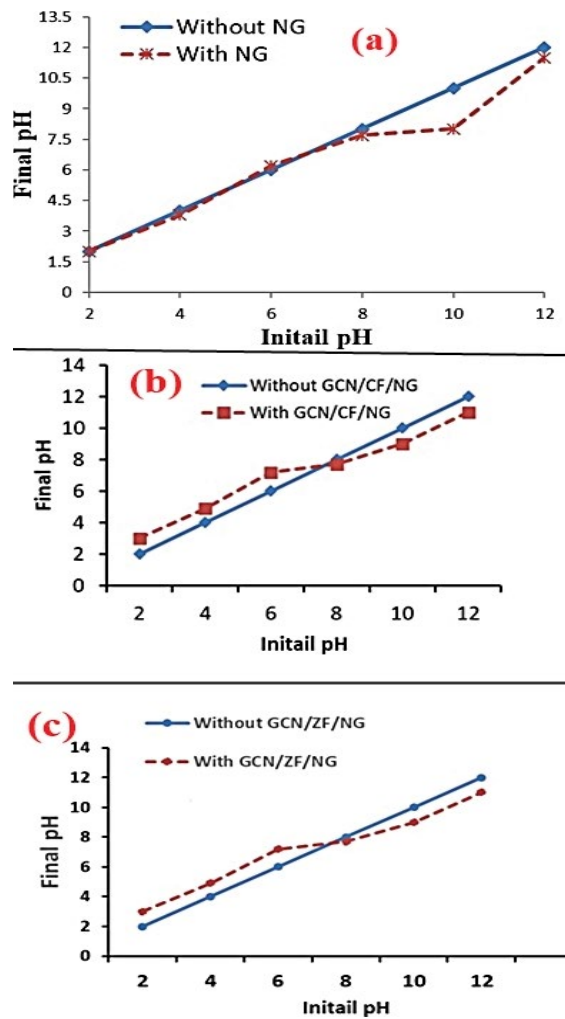


Fig. S3. pH of zero-point charge for (a) NG, (b) GCN/CoFe<sub>2</sub>O<sub>4</sub>/NG, and (c) GCN/ZnFe<sub>2</sub>O<sub>4</sub>/NG photocatalysts.

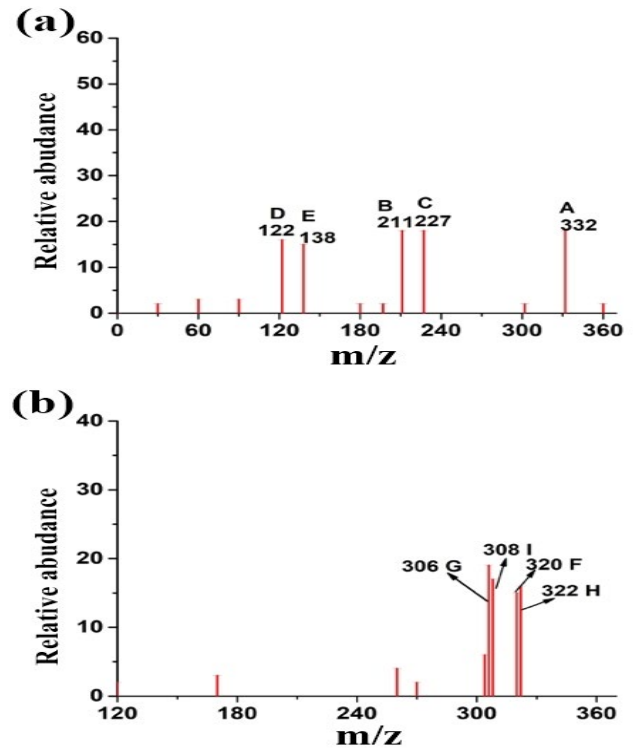


Fig. S4. GC-MS analysis of (a) MG after 70 min and (b) MO after 150 min.

Table S1  
Kinetics for MG and MO onto various adsorbents

	Pseudo-first-order kinetics					
	$k_1$ (min <sup>-1</sup> )		$q_e$ (mg/g)		$R^2$	
	MG	MO	MG	MO	MG	MO
GCN/CoFe <sub>2</sub> O <sub>4</sub> /NG	0.0179	0.0171	66.00	65.12	0.91	0.92
GCN/ZnFe <sub>2</sub> O <sub>4</sub> /NG	0.0173	0.0174	64.56	66.00	0.93	0.90
NG	0.0171	0.0175	60.00	67.10	0.90	0.91
	Pseudo-second-order kinetics					
	$k_2$ (g/mg min)		$q_e$ (mg/g)		$R^2$	
	MG	MO	MG	MO	MG	MO
GCN/CoFe <sub>2</sub> O <sub>4</sub> /NG	0.00025	0.00017	65.12	63.30	0.99	0.96
GCN/ZnFe <sub>2</sub> O <sub>4</sub> /NG	0.00015	0.00011	66.00	64.29	0.96	0.97
NG	0.00005	0.000078	60.00	60.00	0.97	0.98

Reaction condition: [MO] =  $1.5 \times 10^{-5}$  mol dm<sup>-3</sup>; [MG] =  $1 \times 10^{-5}$  mol dm<sup>-3</sup>; [catalyst] = 50 mg/100 mL; pH = 4.0 (MO); 6 (MG); reaction time = 70 min (MG), and 140 min (MO).

Table S2  
Effect of pH of MG and MO adsorption

pH	Removal efficiency of GCN/CoFe <sub>2</sub> O <sub>4</sub> /NG (%)		Removal efficiency of GCN/ZnFe <sub>2</sub> O <sub>4</sub> /NG (%)		Removal efficiency of NG (%)	
	MG	MO	MG	MO	MG	MO
4	15	33	12	34	16	31
6	25	25	20	25	22	30
7	34	17	34	18	30	28
8	35	10	38	10	33	25
9	35	10	38	9	33	22

Reaction parameters: [MO] =  $1.5 \times 10^{-5}$  mol dm<sup>-3</sup>; [MG] =  $1 \times 10^{-5}$  mol dm<sup>-3</sup>; [catalyst] = 50 mg/100 mL; pH = 4.0 (MO); 6 (MG); reaction time = 60 min (MG) and 140 min (MO).

Table S3  
Rate constants for MG and MO photodegradation using photocatalysts

	Photocatalyst	R <sup>2</sup>	k (min <sup>-1</sup> )
MG	GCN/CoFe <sub>2</sub> O <sub>4</sub> /NG	0.99	0.034
	GCN/ZnFe <sub>2</sub> O <sub>4</sub> /NG	0.98	0.032
MO	GCN/CoFe <sub>2</sub> O <sub>4</sub> /NG	0.97	0.026
	GCN/ZnFe <sub>2</sub> O <sub>4</sub> /NG	0.98	0.029

[MO] =  $1.5 \times 10^{-5}$  mol dm<sup>-3</sup>; [MG] =  $1 \times 10^{-5}$  mol dm<sup>-3</sup>; [catalyst] = 50 mg/100 mL; pH = 4.0 (MO); 6 (MG); reaction time = 60 min (MG) and 140 min (MO).